Climatological distribution of dissolved inorganic nutrients in the Western Mediterranean Sea (1981-2017)

Malek Belgacem [1,2]**, Katrin Schroeder** [1]**, Alexander Barth** [3]**, Charles Troupin** [3]**, Bruno Pavoni** [2]**, Patrick Rambault**[4]**, Nicole Garcia**[4]**, Mireno Borghini**[5]**, Jacopo Chiggiato** [1]

[1]CNR-ISMAR, Arsenale Tesa 104, Castello 2737/F, 30122 Venezia, Italy

[2]Dipartimento di Scienze Ambientali Informatica e Statistica, DAIS, Università Ca' Foscari Venezia, Campus Scientifico Mestre, Italy

[3]GeoHydrodynamics and Environment Research, GHER, Freshwater and Oceanic sCiences Unit of reSearch (FOCUS), University of Liège, Quartier Agora, Allée du 6-Août, 17, Sart Tilman, 4000 Liège 1, Belgium

[4]Aix Marseille Université, CNRS/INSU, Université de Toulon, IRD, Mediterranean Institute of Oceanography (MIO) UM 110, 13288, Marseille, France

[5]CNR-ISMAR, La Spezia, Italy

Correspondence: Malek Belgacem (malek.belgacem@ve.ismar.cnr.it)

Abstract

The Western MEDiterranean Sea BioGeochemical Climatology (BGC-WMED) presented here is a product derived from quality controlled in situ observations. Annual mean gridded nutrient fields for the period 1981-2017, and its sub-periods 1981-2004 and 2005-2017, on a horizontal $1/4° \times 1/4°$ grid have been produced. The biogeochemical climatology is built on 19 depth levels and for the dissolved inorganic nutrients nitrate, phosphate and orthosilicate. To generate smooth and homogeneous interpolated fields, the method of the Variational Inverse Model (VIM) was applied. A sensitivity analysis was carried out to assess the comparability of the data product with the observational data. The BGC-WMED has then been compared to other available data products, i.e. the medBFM biogeochemical reanalysis of the Mediterranean Sea and the World Ocean Atlas 2018 (WOA18) (its biogeochemical part). The new product reproduces common features with more detailed patterns and agrees with previous records. This suggests a good reference to the region and to the scientific community for the understanding of inorganic nutrient variability in the western Mediterranean Sea, in space and in time, but our new climatology can also be used to validate numerical simulations making it a reference data product.
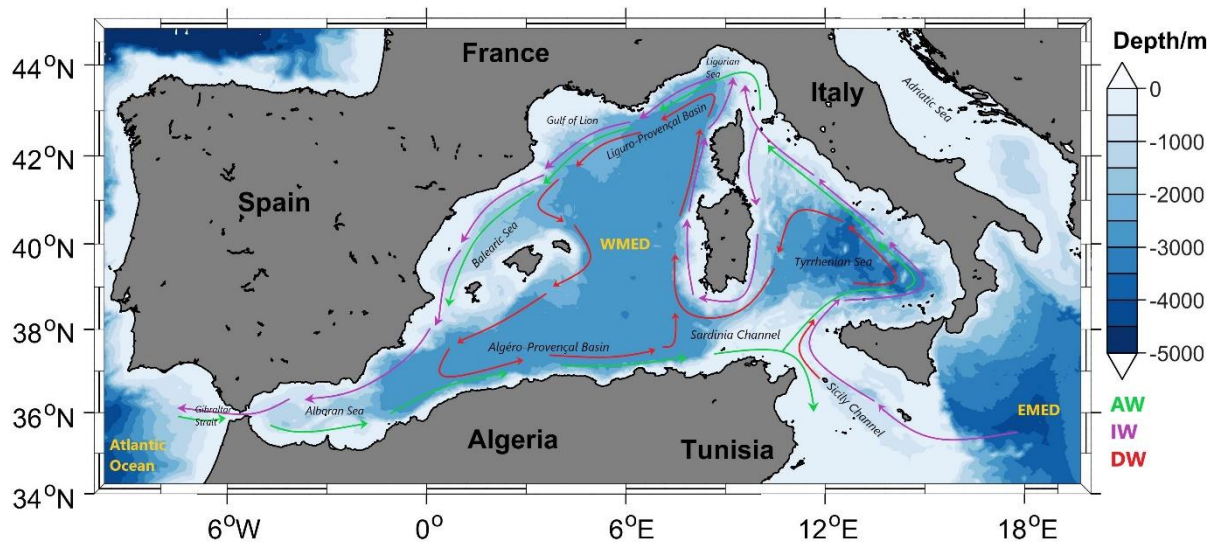
Keywords: Western Mediterranean Sea, climatology, inorganic nutrients, in situ observations.

1 Introduction

Ocean life relies on the loads of marine macro-nutrients (nitrate, phosphate and orthosilicate) and other micro-nutrients within the euphotic layer. They fuel phytoplankton growth, maintaining thus the equilibrium of the food web. These nutrients may reach deeper levels through vertical mixing and remineralization of sinking organic matter. Ocean circulation and physical processes continually drive the large-scale distribution of chemicals (Williams and Follows, 2003) toward a homogeneous distribution. Therefore, nutrient dynamics is important to understand the overall ecosystem productivity and carbon cycles. In general, the surface layer is depleted in nutrients in low latitude regions (Sarmiento and Toggweiler, 1984), but in some ocean regions, called high nutrient low chlorophyll (HNLC) regions, nutrient concentrations tend to be anomalously high, particularly in areas of the North Atlantic and Southern Ocean, as well as in the eastern equatorial Pacific, and in the North Pacific; see e.g. Pondaven et al. (1999). In the Mediterranean, the surface layer is usually nutrient-depleted. Most studies show that nitrate is the most common limiting factor for primary production in the global ocean (Moore et al., 2013), while others evidence that phosphate may be a limiting factor in some specific areas, as is the case of the Mediterranean Sea (Diaz et al., 2001; Krom et al., 2004).

Being an enclosed marginal sea, the Mediterranean Sea exhibits an anti-estuarine circulation, responsible for its oligotrophic character (Bethoux et al., 1992; Krom et al., 2010) and acting like a subtropical anticyclonic gyre. The Atlantic Water (AW), characterized by low-salinity and low-nutrient content, enters the Western Mediterranean Sea (WMED) at the surface, through the Strait of Gibraltar, and moves toward the Eastern Mediterranean Sea (EMED), crossing the Sicily Channel (Fig. 1). In the Levantine and in the Cretan Sea, the AW becomes saltier, warmer and denser, and it sinks to intermediate levels (200-500 m) to form the Intermediate Water (IW, Schroeder et al., 2017). The IW (which may be further called Levantine or Cretan Intermediate Water, LIW or CIW) flows westward across the entire Mediterranean Sea to the Atlantic Ocean (Fig. 1). As for the deep layer, the Western Mediterranean Deep Water (WMDW or DW) is formed in the Gulf of Lion through deep convection (Testor et al., 2018; MEDOC Group, 1970; Durrieu de Madron et al, 2013) while the Eastern Mediterranean Deep Water (EMDW) is formed in the Adriatic Sea and occasionally in the Aegean Sea (Lascaratos et al., 1999; Roether et al., 1996, 2007).

Figure 1. Map of the western Mediterranean Sea showing the main regions with a sketch of the AW, IW and DW major paths.

The Mediterranean Sea is known to be a hotspot for climate change (Giorgi, 2006; Cheng et al., 2021). During the early 1990s, the Deep Water (DW) formation area of the EMED shifted from the Adriatic Sea to the Aegean Sea. This event is known as the Eastern Mediterranean Transient (EMT; Roether et al., 1996, 2007, 2014; Roether and Schlitzer, 1991; Theocharis et al., 2002). As a consequence, the intermediate and deep waters of the EMED became saltier and warmer (Lascaratos et al., 1999; Malanotte-Rizzoli et al., 1999). The EMT affected the WMED as well, not only changing the thermohaline characteristics of the IW and concurring to the preconditioning of the Western Mediterranean Transition (WMT; Schroeder et al., 2016), which set the beginning of a rapid warming and salting of the deep layers in the WMED since 2005 (Schroeder et al., 2006; Schroeder et al., 2010, 2016; Piñeiro at al., 2019). Over the last decade, it has been evidenced that heat and salt content have been increasing all over the deep western basin (Schroeder et al., 2016).

Changes in circulation due to an increased stratification limit the exchange of materials between the nutrient-rich deep layers and the surface layers. Understanding the peculiar oligotrophy of the Mediterranean Sea is still a challenge, since there is not an exact quantification of nutrient sinks and sources. Studies like Crispi et al. (2001), Ribera d'Alcalà (2003), Krom et al. (2010) and Lazzari et al. (2012) related the horizontal spatial patterns in nutrient concentrations mainly to the anti-estuarine circulation which exports nutrients to the Atlantic Ocean, showing a decreasing tendency of nutrient concentrations toward east, as opposed to the salinity horizontal gradient. Others related it to the influence of the atmospheric deposition (Bartoli et al., 2005; Béthoux et al., 2002; Huertas et al., 2012; Krom et al., 2010) and rivers discharges that are rich in nitrate and poor deficient in phosphate (Ludwig et al., 2009), which might explain the peculiarity in both EMED and WMED.

85 Lazzari et al. (2016) also argued that the variations in phosphate are regulated by atmospheric and river
86 inputs like Ebro and Rhône (Ludwig et al., 2009).
87 These variations, together with the anthropogenic perturbations affect the spatial distribution of nutrients
88 (Moon et al., 2016) while temporal variability is still unresolved.

89 De Fommervault et al. (2015) reported a decreasing phosphate and an increasing nitrate concentrations
90 trend between 1990 and 2010, based on a time series (DYFAMED) in the Ligurian Sea, while Moon et
91 al. (2016) evidenced an increase between 1990 and 2005 and a gradual decline after 2005 in both nitrate
92 and phosphate in the WMED and EMED.

93 At the global scale, most of the biogeochemical descriptions are based on model simulations and satellite
94 observations (using sea surface chlorophyll concentrations (Salgado-Hernanz et al., 2019)) but also on
95 the increasing use of Biogeochemical Argo floats (D'Ortenzio et al., 2020; Lavigne, 2015; Testor et al.,
96 2018), since in situ observations of nutrients are generally infrequent and scattered in space and time.
97 For this reason, climatological mapping is often applied to sparse in situ data in order to understand the
98 biogeochemical state of the ocean representing monthly, seasonally, or annually averaged fields.

99 Levitus (1982) was the first to generate objectively analyzed fields of potential temperature, salinity,
100 and dissolved oxygen, and to produce a climatological atlas of the world ocean.

101 Later on, the World Ocean Atlas (WOA), the North Sea climatologies and the Global ocean Carbon
102 Climatology resulting from GLODAP data product (Key et al., 2004, Olsen et al., 2020, Lauvset et al.
103 2021) used the Cressman analysis (1956) with modified Barnes scheme (Barnes 1964, 1994). In 1994,
104 the first World Ocean Atlas (WOA94; Conkright et al., 1994) was released integrating temperature,
105 salinity, oxygen, phosphate, nitrate, and silicate observations. Every four years there is a renewed release
106 of the WOA with an updated World Ocean database (WOD).

107 On the regional scale, the first salinity and temperature climatology of the Mediterranean Sea was
108 produced by Hecht et al. (1988) for the Levantine Basin. Picco (1990) was also among the first to
109 describe the WMED between 1909 and 1987. In 2002, the Medar/Medatlas group (Fichaut et al., 2003)
110 archived a large amount of biogeochemical and hydrographic in situ observations for the entire region
111 and used the Variational Inverse Model (VIM; Brasseur, 1991) to build seasonal and interannual gridded
112 fields. In 2006, the SeadataNet EU project integrated all existing data, to provide temperature and
113 salinity regional climatology products for the Mediterranean Sea using VIM as well (Simoncelli et al.,
114 2016), and dissolved inorganic nutrients (nitrate, phosphate and silicate) 6-years centered average from
115 1965 to 2017 are available on the EMODnet chemistry portal (https://www.emodnet-chemistry.eu/).
116 Within this context, in this study, regional climatological fields of in situ nitrate, phosphate and silicate,
117 using the Data Interpolation Variational Analysis (DIVAnd; Barth et al., 2014) are presented here,
118 providing a high-resolution field contributing to the existing products (Table 1).

119   The aim of this study is to give a synthetic view of the biogeochemical state of the WMED, to evaluate

120   the mean state of inorganic nutrients over 36 years of in situ observations and to investigate upon a

121   biogeochemical signature of the effect of the WMT .

122   The paper is organized as follows, section 2 describes the data sources used and the quality check;

123   section 3 is devoted to the methodology, section 4 presents the main results including a comparison of

124   the new climatology with other products. At the end, we address the change in biogeochemical

125   characteristics before and after WMT.

126   **Table 1.** Overview of the existing inorganic nutrient climatologies in the Western Mediterranean Sea.

Climatology	WOA	EMODnet	BGC-WMED (Present study)
Reference	(Garcia et al., 2019)	(Míguez et al., 2019)	(Belgacem et al., 2021)
Year of release	2018	2018	2021
Parameter	Nitrate/ Phosphate/ Silicate	Nitrate/ Phosphate/ Silicate	Nitrate/ Phosphate/ Silicate
Unit	μmol kg^{-1}	μmol L^{-1}	μmol kg^{-1}
Data type	CTD Bottle	CTD Bottle	CTD Bottle
Vertical resolution	Seasonal: 43 levels 0-800m Annual: 102 levels 0-5500m	21 standard depths 0-1100m (nitrate) 0-1500m (phosphate) 0-1500m (silicate)	19 levels 0-1500m
Horizontal resolution	1° latitude longitude grid	1/8°	1/4°
Observation time span	1955-2017	1970 to 2016 (nitrate) 1960 to 2016 (phosphate) 1965 to 2016 (silicate)	1981-2017
Area	Global	Mediterranean Sea	Western Mediterranean Sea
Temporal resolution	Season Decadal	Season 6 year running averages	whole observational period, and two sub-intervals (1981-2004, 2005-2017)
Climatology analysis method/ parameter	Objective analysis	DIVA (Data-Interpolating Variational Analysis) tool	DIVAnd (Data-Interpolating Variational Analysis N-dimension)
Correlation length	-	optimized and filtered vertically and a seasonally averaged profile was used.	optimized and filtered vertically and horizontally
Signal to noise ratio	-	A constant value = 1	A constant value = 0.5
Background field	-	the data mean value is subtracted from the data.	the data mean value is subtracted from the data
Detrending	-	No	No
Advection constraint applied	-	No	No

127

128   **2 Data**

129   The climatological analysis depends on the temporal and spatial distribution of the available in situ data,

130   and the reliability of these observations. Due to the scarcity of biogeochemical observations in the

131   WMED, merging and compiling data from different sources was necessary.

132 2.1 Data Sources

133 In total, 2253 in situ inorganic nutrient profiles are the base of the biogeochemical climatology of the

134 WMED (Table 2) that is described here. These profiles cover the period 1981-2017 and come from the

135 major data providers existing in the Mediterranean Sea, i.e. the Medar/MEDATLAS (1981-1996,

136 Fichaut et al., 2003), the recently published CNR_DIN_WMED_20042017 biogeochemical dataset

137 (2004-2017) (Belgacem et al., 2020), the MOOSE-GE cruises (Mediterranean Ocean Observing System

138 for the Environment- Grande Échelle programme) (2011-2016, Testor et al., 2011, 2012, 2013, 2014,

139 2015, 2016) stored in SeaDataNet data product (2001-2016) and EMODnet (the European Marine

140 Observation and Data Network), GLODAPv2 (https://www.glodap.info/) and CARIMED

141 (http://hdl.handle.net/10508/11313) data products and other data collected during MedSHIP programs

142 (Schroeder et al., 2015) . All datasets are a selection of oceanographic cruises carried out within the

143 framework of European projects such as the HYdrological cycle in the Mediterranean Experiment

144 (HyMeX) Special Observing Period 2 (Estournel et al., 2016), the DEnse Water Experiment (DEWEX)

145 project or by regional institutions having as objectives the investigation of the deep water convection

146 and the biogeochemical properties of the of the WMED. Data were chosen to ensure high spatial

147 coverage (Fig. 3).

148 **Table 2.** Number of inorganic nutrient profiles and data sources.

Source	N. of profiles	N. of observations	Link/ metadata
MEDATLAS	940	8839	http://www.ifremer.fr/medar/
SEADATANET including MOOSE-GE	523	15388	http://seadatanet.maris2.nl/v_rsm/content.asp?screen=0&history=yes https://doi.org/10.17600/11450160 https://doi.org/10.17600/12020030 https://doi.org/10.17600/13450110 https://doi.org/10.17600/14002300 https://doi.org/10.17600/15002500 https://doi.org/10.17600/16000700
CNR_DIN_WMED_20042017	737	8324	https://doi.org/10.1594/PANGAEA.904172
Other cruises	53	515	Medship programs; GLODAPv2; CARIMED (not yet available online, personal communication by Marta Álvarez) https://doi.org/10.1594/PANGAEA.902293
∑	*2253*	33066	-

149

150 2.2 Data distribution

151 The data distribution per year is shown in Figure 2a. Most observations were collected between 1981

152 and 1995, and between 2004 and 2017, with a marked gap between 1997 and 2003. Measurement

153 distribution differs from month to month (Fig.2b) and tends to be biased towards the warm season. Very

154 few measurements have been made during December-January-February, while June and July are the

155 months with the highest number of available observations (>7000). Consequently, the climatological

156 product may be considered as being more representative of spring and summer conditions.
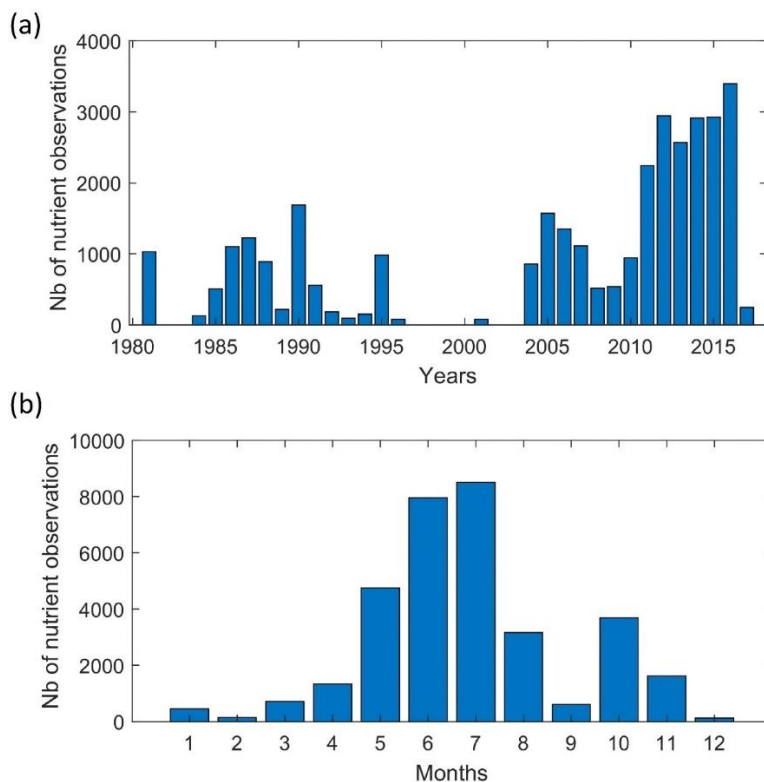
157

158 **Figure 2**. Temporal distribution of nutrient observations used for producing the BGC-WMED fields

159 (1981-2017), (a) yearly distribution and (b) monthly distribution.

160 Fig. 3a shows the regional distribution of nutrient measurements, while Fig. 3b indicates the number of

161 observations found in each depth range around the standard levels chosen for the vertical resolution of

162 the climatology.

163 Hydrological and biogeochemical measurements have always been repeatedly collected along several

164 repeated transects, known as key regions as the Sicily Channel and the Algéro-Provençal subbasin;

165 likewise, the northern WMED is a well sampled area, as it is an area of DW formation. Observation

166 density is still scarce (less than 100 observations) in some areas like the northern Tyrrhenian Sea.

167 The total number of measurements at each depth range underlines similar remarks, an uneven

168 distribution that needs to be considered in the selection of the vertical resolution to estimate the

169 climatological fields. Though, the use of 36 years of nutrient measurements to generate the

170 climatological fields significantly reduces the error field. In our case and taking into account the irregular

171 distribution in seasons and different years. A climatological gridded field was computed by analyzing

172 observations of three time periods regardless of the month: 1981-2017 and the subsets 1981-2004 and

173 2005-2017. We chose these subsets to investigate the effect of the WMT on nutrient distribution.

7
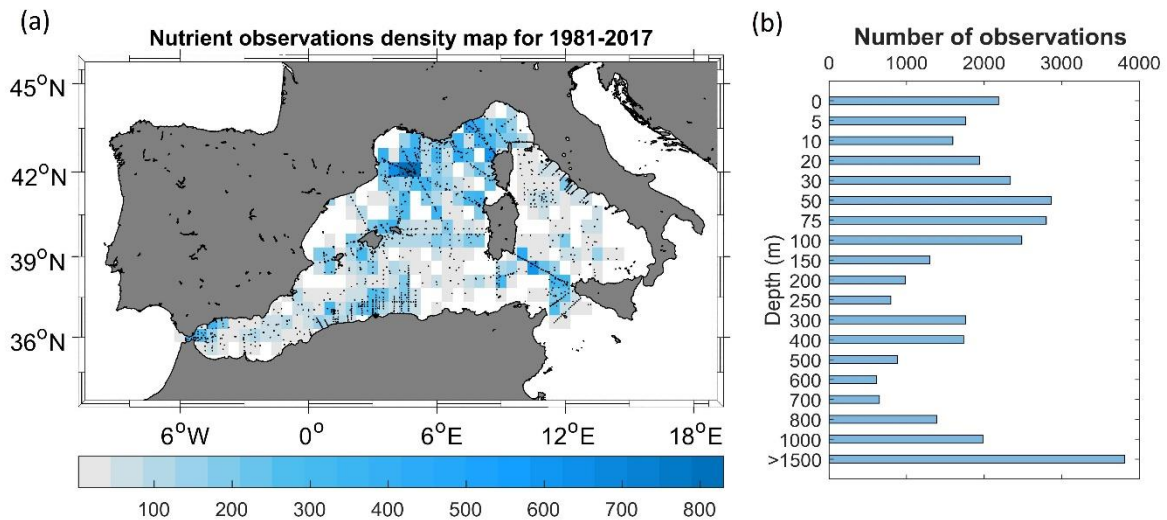
Figure 3. (a) Nutrient data density used for climatology analysis. Observations are binned in a regular $1/2° \times 1/2°$ latitude, longitude grid for each year over the period 1981-2017. Location of the stations included in the analysis are shown as black dots; (b) data distribution per depth range (i.e. at 800 m, observations between 800-1000 m are included).

2.3 Data quality check

Data were gathered from different data sources, different analytical methods (Table A1.), thus before merging them, observations were first checked for duplicate (the number of profiles listed in Table 2 refers to all data after removing duplicate measurements). The criteria to detect and remove duplicates is simple: observations collected during the same cruises extracted from the different sources were removed. Since profiles were measured during specific cruise (identified with a unique identification code) at specific time, data from duplicate cruises are removed.

Then, data was converted to a common format (similar to the csv CNR_DIN_WMED_20042017 data product, Belgacem et al., 2019). This recently released product contains measurements covering the WMED from 2004 to 2017. The data of the CNR_DIN_WMED_20042017 product have undergone a rigorous quality control process that was focused on a primary quality check of the precision of the data and a secondary quality control targeting the accuracy of the data, details about the adjustments and the applied corrections are found in Belgacem et al.(2020).

As detailed in Table 2, we combined observations from reliable sources (covering the time period 1981-2017), that were quality controlled according to international recommendations before being published (Maillard et al., 2007; SeaDataNet Group, 2010). Though, these historical data collections coming from sources different from the CNR_DIN_WMED_20042017 have been subjected to a quality check before merging them, to eliminate the effect of any aberrant observation. The check was carried out by computing median absolute deviations in 19 pressure classes (referring to the selected vertical resolution

8

198 of section 2.1, Fig.3b) (0-10, 10-30, 30-60, 60-80, 80-160, 160-260, 260-360, 360-460, 460-560, 560-
199 900, 900-1200, 1200-1400, 1400-1600, 1600-1800, 1800-2000, 2000-2200, 2200-2400, 2400-2600,
200 >2600 dbar). Any value that is more than three median absolute deviations from the median value is
201 considered a suspected measurement.

202 In total, 2.35% of nitrate observations, 2.44% of phosphate observations and 2.14% of silicate
203 observations were removed.
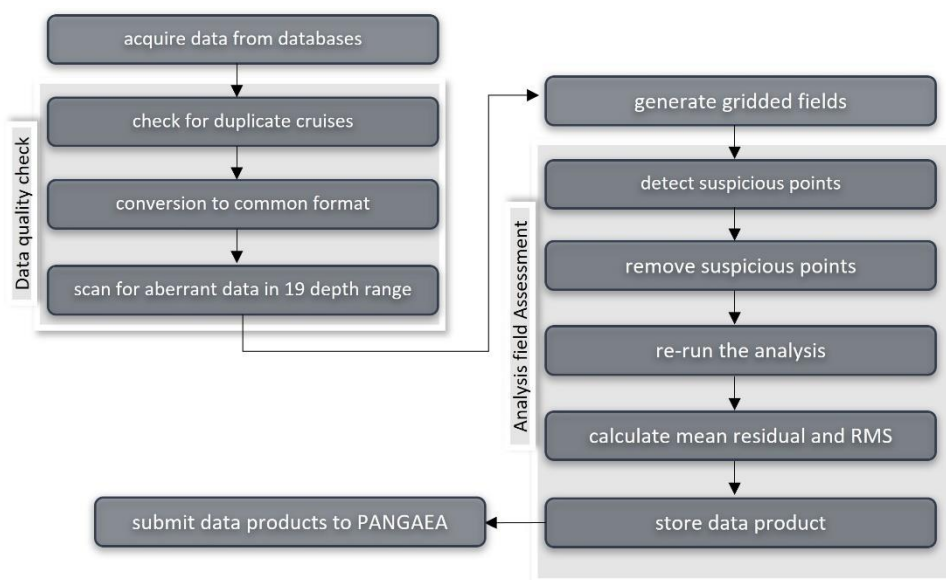
204

205 **Figure 4.** Flowchart describing the steps during the quality control; see text in section 2.3 and 3.3 for
206 more details.

207 **3 Methods**

208 3.1 Variational analysis mapping tool

209 Here, the **D**ata-**I**nterpolating **V**ariational **A**nalysis- **n d**imension (DIVAnd) method (Beckers et al., 2014;
210 Troupin et al., 2010, 2012) was used to generate the gridded fields. DIVA has been widely applied to
211 oceanographic climatologies, such as the SeaDataNet climatological products (Simoncelli et al., 2014,
212 2016, 2019, 2020a, 2020b, 2020c, 2021; Iona et al., 2018), EMODnet chemistry regional climatologies
213 (Míguez et al., 2019), the Adriatic Sea climatologies by Lipizer et al. (2014) or the black Sea (Capet et
214 al., 2014) and it was also applied to generate the global interior climatology GLODAPv2. 2016b
215 (Lauvset et al., 2016). It is an efficient mapping tool used to build a continuous spatial field from
216 discrete, scattered, irregular in situ data points with an error estimate at each level.

217 The BGC-WMED gridded fields have been computed with the more advanced N-dimensional version
218 of DIVA, DIVAnd v2.5.1 (Barth et al., 2014) (https://doi.org/10.5281/zenodo.3627113) using Julia as

9

219   a programming language (https://julialang.org/) under the Jupyter environment (https://jupyter.org/).

220   The code is freely available at https://github.com/gher-ulg/DIVAnd.jl (last access: January, 2020).

221   DIVA is based on the variational inverse method (VIM) (Brasseur et al., 1996). It takes into account the

222   errors associated with the measurements and takes account of the topography/bathymetry of the study

223   area. The method is designed to estimate an approximated field φ close to the observations and find the

224   field that minimizes the cost function $J[\varphi]$.

225   The cost function is defined as the misfit between the original data d_i, an array of N_d observations, the

226   analysis (observation constraint term) and a smoothness term. (Troupin et al., 2010):

227    $$J[\varphi] = \sum_{i=1}^{Nd} \mu_i Lc^2 \big(d_i - \varphi(x_i, y_i)\big)^2 \qquad (1)\ Observation\ constraint\ term$$

228    $$+ \int_D \big(\alpha_2 \nabla\nabla_\varphi : \nabla\nabla_\varphi + \alpha_1 Lc^2 \nabla_\varphi . \nabla_\varphi + \alpha_0 Lc^4 \varphi^2\big) dD \qquad (2)\ Smoothness\ term$$

229

230   Eq. (1)

231   where Lc is the correlation length, ∇ is the gradient operator, $\nabla\nabla_\varphi : \nabla\nabla_\varphi$ is the squared Laplacian of φ,

232   the first term (observation constraint) considers the distance between the observations and the analysis

233   reconstructed field $\varphi(x_i, y_i)$, so that μ_i penalizes the analysis misfits relative to the observations. if the

234   observation constraint is only composed of $d_i - \varphi(x_i, y_i)$, the constructed field would be a simple

235   interpolation of the observations and the minimum is reached when $d_i = \varphi(x_i, y_i)$. The field $\varphi(x_i, y_i)$

236   need to be close to the observation and not have large variation. The second term (smoothness term)

237   measures the regularity of the domain of interest D. This expression within the integral remains

238   invariant (Brasseur and Haus, 1991). α_0 minimize the anomalies of the field itself, α_1 minimize the

239   spatial gradients, α_2 penalizes the field variability (regularization). The reconstructed fields are

240   determined at the elements of a grid on each isobath using the cost function Eq. (1).

241   The grid is dependent on the correlation length and the topographic contours of the specified grid in the

242   considered region, so there is no need to divide the region before interpolating.

243   The method computes two-, three- to four-multi-dimensional analyses (longitude, latitude, depth, time).

244   For climatological studies, the four-dimensional extension was used on successive horizontal layers at

245   different depths for the whole time period.

246   Along with the gridded fields, DIVA yields error fields dependent on the data coverage and the noise in

247   the measurements (Brankart and Brasseur, 1998; Rixen et al., 2000). Full details about the approach are

248 provided extensively by Barth et al. (2014) and Troupin et al. (2018) in the Diva User Guide
249 (https://doi.org/10.5281/zenodo.836723).

250 3.2 Interpolation parameters

251 DIVAnd is conditioned by topography, by the spatial correlation length (Lc) and by the signal-to-noise
252 ratio (SNR, λ) of the measurements, which are essential parameters to obtain meaningful results. They
253 are considered more in detail in the following sections.

254 3.2.1 Land-sea mask

255 A 3D dimension land-sea mask is created using the coastline and bathymetry of the General Bathymetric
256 Chart of the Oceans (GEBCO) 30-sec topography (Weatherall et al., 2015). The WMED is a relatively
257 small area which necessitates a high-resolution bathymetry to generate a mask at different depth layers.
258 The vertical resolution is set to 19 standard depth levels from the surface to 1500 m: 0, 5, 10, 20, 30, 50,
259 75, 100, 150, 200, 250, 300, 400, 500, 600, 700, 800, 1000, 1500 m, corresponding to the most
260 commonly used predefined levels for the sampling of seawater for nutrient analyses. The resulting fields
261 at each depth level are the interpolation on the specified grid. These depth surfaces are the domain on
262 which the interpolation is performed.

263 3.2.2 The spatial correlation length scale (Lc)

264 Lc indicates the distance over which an observation affects its neighbors. The correlation length can be
265 set by the user or computed using the data distribution.

266 For the BGC-WMED biogeochemical climatology, this parameter was optimized for the whole-time
267 span, and at each depth layer. The correlation length has been evaluated by fitting the empirical kernel
268 function to the correlation between data isotropy and homogeneity in correlations. The quality of the fit
269 is dependent on the number of observations (Troupin et al., 2018). The analytical covariance model used
270 in the fit is derived for an infinite domain (Barth et al, 2014). To assess the quality of the fit, the data
271 covariance and the fitted covariance are plotted against the distance between data points (Fig. 5). At 10
272 m, the correlation length was obtained with a high number of data points, indicating that the empirical
273 covariance used to estimate the covariance and the fitted covariance are in good agreement.

274 At some depth layers there are irregularities due to an insufficient amount of data points, making it
275 necessary to apply a smoothing filter/fit to minimize the effect of these irregularities. It has been tested
276 whether a randomly selected field analysis (nitrate data from 2006 and 2015) obtained with the fitted-
277 vertical correlation profile is better than the analysis with zero-vertical correlation. A skill score relative
278 to analysis non-fitted-vertical correlation has been computed following Murphy (1988) and Barth et al.
279 (2014):

$$skill\ score = 1 - \frac{RMS^2_{no\ fit}}{RMS^2}$$ Eq. (2)

A large difference in the global RMS between the analysis with the fitted-vertical correlation and the analysis with non-fitted-vertical correlation used for validation was found. The test shows whether the use of the fit in the correlation profile is improving the overall analysis or not. We found that the RMS error (nitrate analysis of 1981-2017) was reduced from 0.696 μmol kg^{-1} (analysis without fit) to 0.571 μmol kg^{-1} (analysis with fit) at 10 m depth, which means using the fitted vertical correlation profile in the analysis improves the skill by 32 %, and the fit is improving the analysis fields.
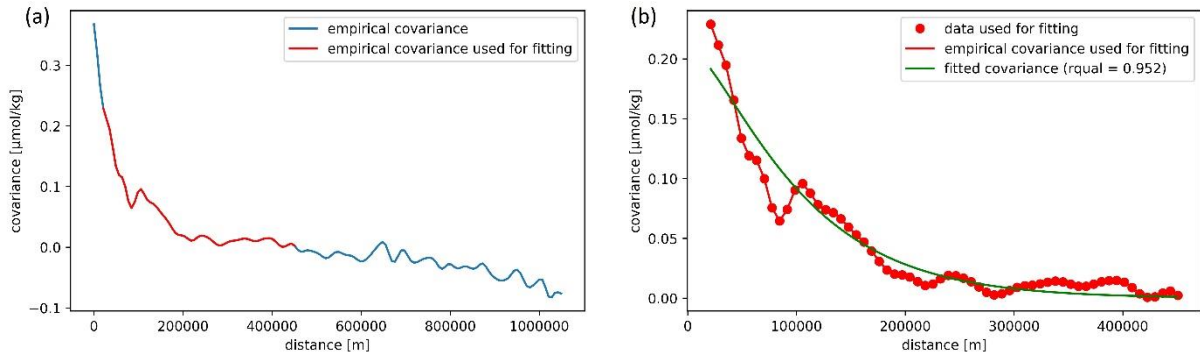
Figure 5. Example of the Nitrate covariance. (a) The empirical data covariance function is given in red, the curve comes from the analysis of observations within depth = 10 m, while (b) the fitted covariance curve (theoretical kernel) is given in green.

Based on the data, DIVA performs a least-square fit of the data covariance function with a theoretical function. Then, a vertical filter is applied and an average profile over the whole period is used (Fig. 6). This procedure is analogous to what has been used for the EMODnet climatology and the North Atlantic climatology, except that in EMODnet climatology, seasonally averaged profiles were used (Buga et al., 2019) and a monthly averaged profiles were used in North Atlantic climatology (Troupin et al., 2010). The filter is applied to discard aberration caused by outliers or scarce observations in some layers, as described above.

Because of the horizontal and vertical inhomogeneity of the data coverage, the analysis was based on a correlation length that varies both horizontally (Fig. 6a) and vertically (Fig. 6b).

As expected, Lc increases with depth (Fig. 6), extending the influence area of the observation, a consequence of the fact that variability at depth is lower and that observations in the deep layer are scarcer (which on the other hand makes the Lc estimate more uncertain).

From the surface to 150-200 m, Lc is rather constant (Fig. 6), while from 200 to 600 m, the horizontal Lc (Fig. 6a) increases for all nutrients. Below 600 m, the horizontal Lc for silicate decreases down to 1000 m, and then increases again at 1500 m. For nitrate and phosphate, a similar, but less marked, behavior is observed.

The vertical Lc (Fig. 6b) behaves similarly toward the increase, for nitrate and phosphate, due to the homogeneity of the intermediate water mass, as explained also by Troupin et al. (2010). For silicate, the vertical Lc decreases in the intermediate depth, reaching a minimum at 500 m depth. The different behavior of silicate could be explained by the progressive increase in concentrations from the surface to the deep layer, compared to nitrate and phosphate vertical distribution (strong gradient between surface depleted layer and intermediate layer). Lc for silicate has lower values compared to nitrate and phosphate, because, horizontally and vertically, it behaves in a different way. Unlike nitrate and phosphate, silicate does not show a strong east-west increased gradient. This gradient might induce this difference in the horizontal distance over which the sample influences its neighborhood.

Besides, silicate is less utilized by primary producers, and the dissolution of the biogenic silica is slower than that of the other nutrients (DeMaster, 2002) which explain its progressive increase towards deeper layers (Krom et al., 2014). The vertical Lc for all nutrients increases progressively from 400 m to 1500 m.

Troupin et al. (2010) and Iona et al. (2018) attributed similar changes observed in Lc for temperature and salinity to the variability of the water masses in each layer. This might also explain the changes found in Lc for nutrients. Indeed, the concentration of nutrients in the WMED increases with depth and is very low at the surface, which explains the constant low values of Lc in this layer.
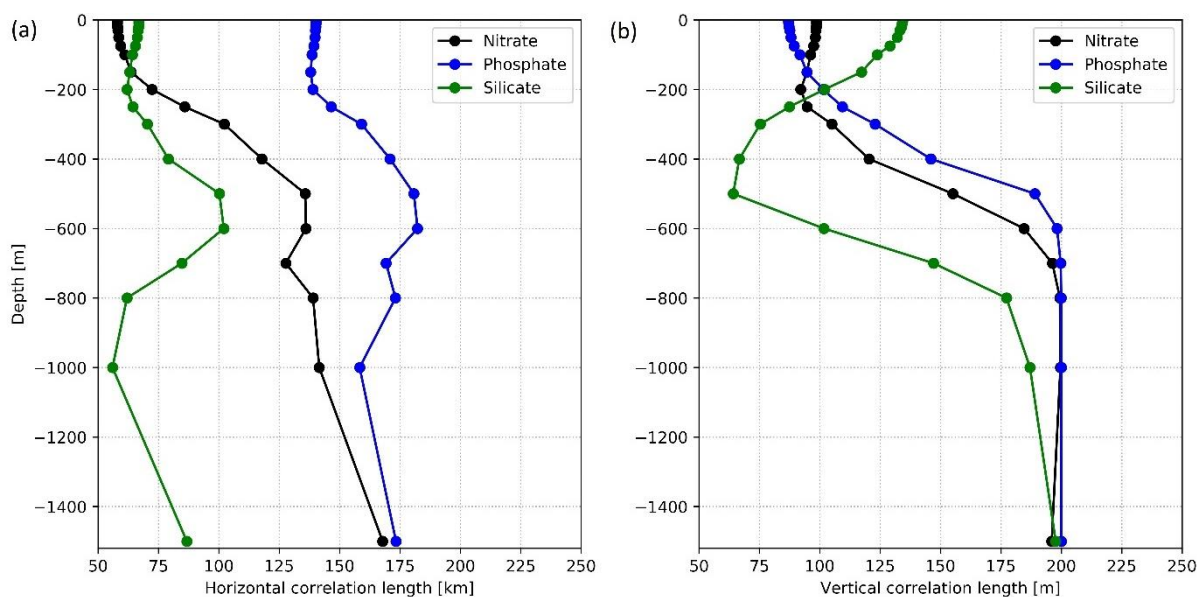
Figure 6. (a) Horizontal and (b) vertical optimized correlation lengths, for each nutrient (1981-2017), as a function of depth.

3.2.3 Signal-to-Noise Ratio

The signal-to-noise ratio (SNR) is related to the confidence in the measurements. It is the ratio between the variance of the signal and the variance of the measurement noise/error. The SNR defines the

330 representativeness of the measurements relative to the climatological fields, in other words, it is the
331 confidence in the data.

332 It not only depends on the instrumental error but also on the fact that observations are instantaneous
333 measurements, and since a climatology is a long-term mean, such observations do not represent exactly
334 the same.

335 Generally, small SNR values favor large deviations from the real measurements to give a smoother
336 climatological field. On the other hand, with a high SNR, DIVAnd keeps the existing observations and
337 interpolates between data points. The need is to find an approximation that does not deviate much from
338 the real observations (further details in Lauvset et al., 2016, and Troupin et al., 2010).

339 Following the same approach that many climatologies that used the DIVAnd method adopted, i.e.
340 EMODnet climatologies (available on the EMODnet chemistry portal), the Atlantic regional
341 climatologies (Troupin et al., 2010), the Adriatic Sea climatology (Lipizer et al., 2014) and the
342 SeadataNet regional climatology (Simoncelli et al., 2015), the SNR is set to a constant value (Table 1).

343 The analysis is performed with a predefined uniform default error variance of 0.5 for all parameters at
344 all depths, we presume that the data sources used to generate BGC-WMED climatology are consistent
345 products. Three iterations are done inside DIVAnd to estimate the optimal scale factor of error variance
346 of the observation (following Desroziers et al., 2005). More details can be found in https://gher-
347 ulg.github.io/DIVAnd.jl/latest/#DIVAnd.diva3d.

348 Values of SNR provided by means of a generalized cross-validation (GCV) technique (Brankart and
349 Brasseur, 1998) gave a large estimate of the SNR (of the order of 22) showing a discontinuous analysis
350 field and patterns around the cruise transects that do not represent properly the climatological fields.

351 3.3 Detection of suspicious data

352 Assessment of the analysis is performed by detecting outliers and suspicious data , in order to remove
353 observations that generate irregular interpolated fields; and suspect observations that were not detected
354 in the data quality check of section 2.3.

355 The automatic check measures how consistent the gridded field is, with respect to the nearby
356 observations, by estimating the difference between a measurement and its analysis scaled by the
357 expected error; based on that, a score is assigned to each observation. Data points with the highest scores
358 were considered as suspect and were removed from the analysis (Fig. A1, A2, A3). Overall, 0.031%,
359 0.014%, 0.004% data points, for nitrate, phosphate, and silicate, respectively, were considered
360 inconsistent. Details about the quality check values and range are plotted in the appendix (Table A1).

361   3.4 Quality check of the analysis fields

362   The quality of the climatology was checked against observations by estimating the mean residual and
363   the root mean squared (RMS) of the difference between the climatology and the observations. Averages
364   over the entire basin were calculated between depth surfaces (see section 2.3). Residuals are the
365   difference between the observations within the specific depth surface and the analysis (interpolated
366   linearly to the location of the observations) and are estimated by depth range (Fig. 7). The analysis fields
367   at each depth range (i.e. depth surfaces or domain on which the interpolation is performed) are the
368   interpolation on the specified grid. In Fig. 7, we present the vertical profile of the mean residuals and
369   RMS at different depth ranges for the three nutrients.

370   Nitrate observations and the analysis field in Fig.7a have a high level of agreement in the surface layer
371   (from 0 to 30 m depth). Just below (between 30 and 200 m), boxplots are suggestive of larger differences.
372   From surface to the deep layer, the mean residual between nitrate observation and the gridded field
373   varied between -0.075 and 0.0765 μmol kg^{-1}, while the corresponding RMS fluctuated between 0.47 and
374   1.1 μmol kg^{-1}. This is justified by the inhomogeneity of the observations mainly in deep layers.

375   As for the average residual between phosphate observations and the gridded analysis (Fig.7b), it was
376   around zero and varied between -0.0027 and 0.0026 μmol kg^{-1}. The RMS for phosphate was between
377   0.037 and 0.063 μmol kg^{-1}.

378   Silicate residuals (Fig. 7c), on the other hand, seemed more homogeneous at all depth levels. The highest
379   level of agreement was found below 20 m and at 600 m. Overall, residuals varied between -0.057 and
380   0.063 μmol kg^{-1}, while the RMS ranged between 0.567 and 0.963 μmol kg^{-1}.

381   Over the entire water column, the mean residual was around zero (0.004 μmol kg^{-1} for nitrate, 0.0002
382   μmol kg^{-1} for phosphate and 0.003 μmol kg^{-1} for silicate) (Fig. 7). The RMS (in blue line) fell within the
383   mean residual +/- standard deviation in the upper 25th percentile at the different depth ranges and in all
384   parameters meaning that in general, the bias between the observations and the analysis is small and there
385   is a good agreement.
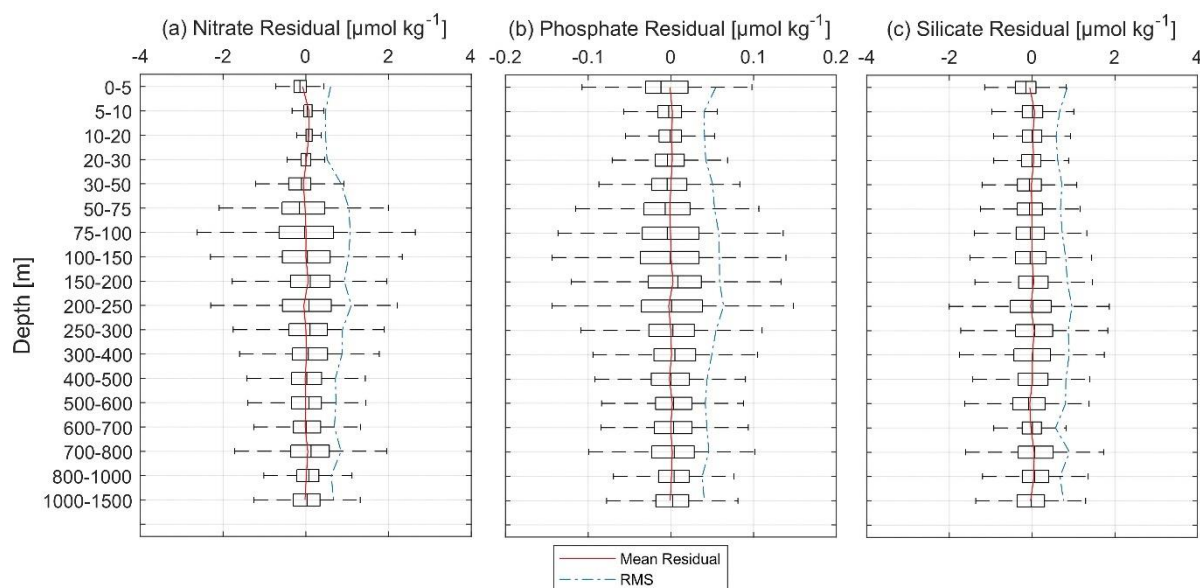
Figure 7. Vertical mean residuals (in red), i.e. the differences between the observations and the analysis, and the mean RMS (dashed blue) of (a) nitrate, (b) phosphate, (c) silicate.

4 Results

The final result consists of gridded fields of mapped climatological means of inorganic nutrients for the periods 1981-2004, 2005-2017, and the whole period 1981-2037, produced with VIM described in section 3, using data of section 2. Together with the gridded fields, error maps have been generated to check the degree of reliability of the analysis.

The resulting climatologies (Table 3) are aggregated in a 4D netCDF for each nutrient and each time period that contains the interpolated field of the variable and the related information: associated relative error, variable fields masked using two relative error thresholds (L1 and L2). The mapped climatology is available from PANGAEA (https://doi.pangaea.de/10.1594/PANGAEA.930447, Belgacem et al., 2021) as one folder named BGC-WMED climatology. This folder contains nine files: three per parameter and three per time period.

Here is an example of the analysis output found in the netCDF. Figure 8 shows the unmasked climatological field of the mean spatial variation of nitrate, relative error field distribution, the masked climatological field using relative error with two threshold values (0.3 and 0.5) to assess the quality of the resulting fields.

16

Table 3. Available analyzed fields and related information in the netCDF files.

Variable name	Field name	Description
Lon	Longitude	Longitude in degrees east, extent: -7 – 17.25 °E
Lat	Latitude	Latitude in degrees north, extent: 33.5 – 45.85°N
depth	Depth	Depth in meters, 19 levels, range: 0 – 1500 m
nitrate/phosphate/silicate	DIVAnd analyzed climatology	Mapped climatological fields
nitrate_L1/phosphate_L1/ silicate_L1	Nitrate/Phosphate/Silicate masked field level 1	Mapped climatological fields masked using relative error threshold 0.3.
nitrate_L2/ phosphate_L2/ silicate_L2	Nitrate/Phosphate/Silicate masked field level 2	Mapped climatological fields masked using relative error threshold 0.5.
nitrate_relerr/phosphate_re lerr/silicate _relerr	Nitrate/Phosphate/Silicate masked relative error	Mapped relative error fields associated to the climatological field

408

409
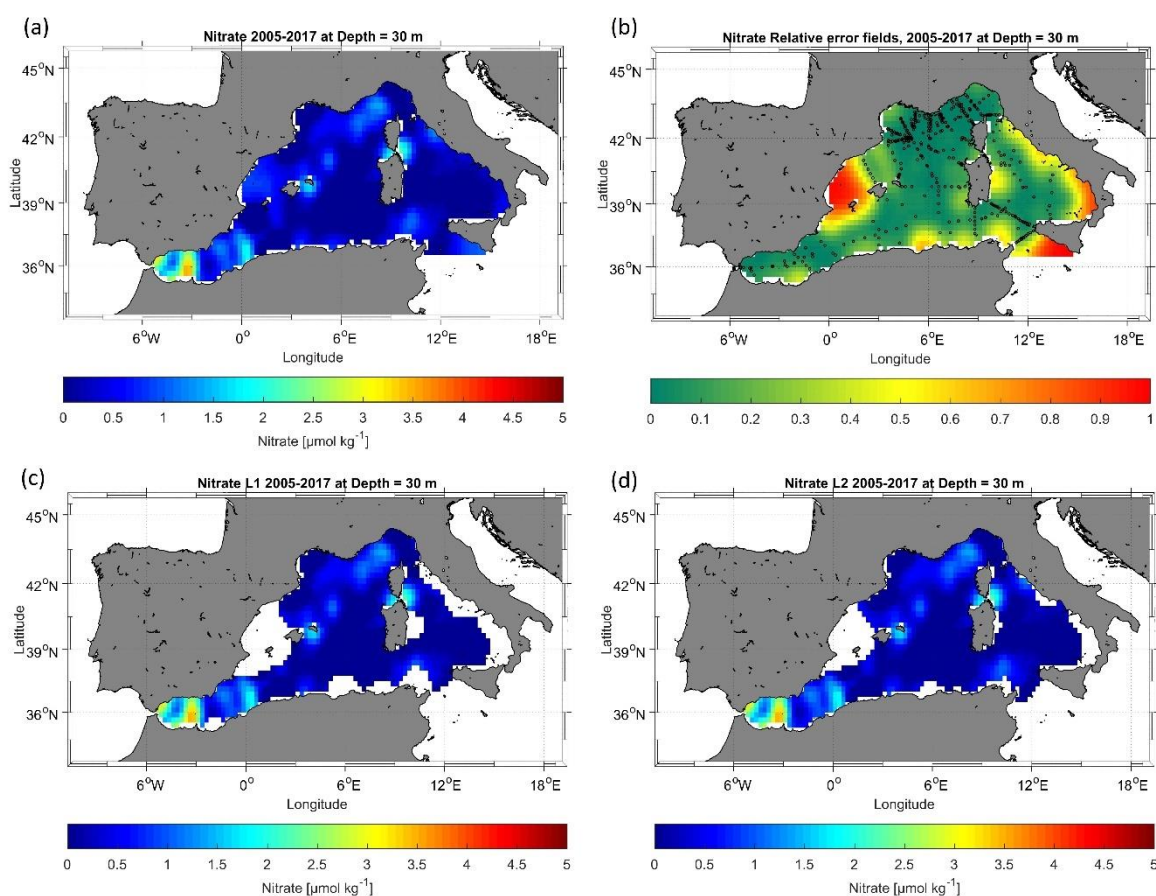
Figure 8. Example of nitrate analysis for the period 2005-2017 (a) unmasked analysis field, (b) relative error field distribution with the observation in black circles, (c) masked analysis fields masked using relative error threshold = 0.3, and (d) masked analysis fields masked using relative error threshold = 0.5.

4.1 Nutrient climatological distribution

A description of the spatial patterns of the dissolved inorganic nutrients across the domain and over the entire period (1981-2017) is given. The gridded fields for nitrate, phosphate, and silicate are discussed at three depth levels, representative of the surface (at 100 m), intermediate (at 300 m), and deep layer

417   (at 1500 m). The horizontal maps at the selected depths are shown in Fig. 9, while the average vertical

418   profiles of nutrients over the whole area are shown in Fig. 10.

419   4.1.1 Surface layer

420   The nitrate, phosphate and silicate mean climatological fields over 1981-2017 are presented in Fig. 9 (a,

421   b, c) respectively. The mean surface nitrate at 100 m is about 3.58 ± 1.16 μmol kg^{-1}. Highest surface

422   values of nitrate concentrations are found in regions where strong upwelling or vertical mixing occurs,

423   such as the Liguro-Provençal basin and the Alboran Sea (see Fig. 9a), and regions with extensive supply

424   by the Ebro, Rhone, Moulouya and Chelif rivers.

425   The convection region (Gulf of Lion and Ligurian Sea) is characterized by an eutrophic regime and a

426   spring bloom (Lavigne et al., 2015), unlike the rest of the basin that shows low nitrate concentrations in

427   the surface layer (< 4 μmol kg^{-1}).

428   Nutrient patterns in the Alboran Sea have been associated with the distinct vertical mixing that supplies

429   the surface layer with nutrients (Lazzari et al., 2012; Reale et al., 2020).

430   Indeed, the northern Alboran Sea is known as an upwelling area, where permanent strong winds enhance

431   the regional biological productivity (Reul et al., 2005). Nitrate distribution at 100 m presents a clear

432   distinction between the enriched surface regions in the WMED, under the influence of deep convection

433   processes, and the easternmost depleted regions.

434   The distribution of phosphate concentration has striking similarities with that of nitrate (Fig. 9b). The

435   mean surface phosphate concentration at 100 m, is 0.16 ± 0.06 μmol kg^{-1}. As for nitrate, the highest

436   surface values are found in the Alboran Sea, Balearic Sea, Gulf of Lion and Liguro-Provençal Basin

437   (0.2-0.3 μmol kg^{-1}), while the Tyrrhenian Sea and the Algerian Sea revealed phosphate concentrations

438   that were <0.2 μmol kg^{-1}. Similar patterns were observed by Lazzari et al. (2016), who argued that the

439   variations in phosphate are regulated by atmospheric and terrestrial inputs. It should be noted that the

440   maximum in the surface is found near river discharges of freshwater, like Ebro and Rhône, i.e. the largest

441   rivers of the WMED (Ludwig et al., 2009).

442   Concerning the distribution of silicate concentration, the surface layer at 100 m (Fig. 9c) followed the

443   same pattern as nitrate and phosphate. Over this layer the mean silicate was about 2.7 ± 0.7 μmol kg^{-1}.

444   As for nitrate and phosphate, the highest values (3-4 μmol kg^{-1}) were recorded in the Alboran Sea,

445   Balearic Sea, Gulf of Lion and Liguro-Provençal Basin and in the southern entrance of the Tyrrhenian

446   Sea. This surface distribution is in good agreement with the findings of Crombet et al. (2011), relating

447   this local silicate surface maximum to the continental input, river discharge and atmospheric deposition

448   (Frings et al., 2016; Sospedra et al., 2018). The spatial minima were reported in the Tyrrhenian Sea and

449   in the Algerian Sea (<3 μmol kg^{-1}).

450   4.1.2 Deep and Intermediate layer

451   At the basin scale, nitrate concentrations increase with depth (Fig. 10a), with the highest concentration

452   found at intermediate levels (250-500 m), ranging between 8.8 and 9.0 μmol kg^{-1}. In this 300 m layer

453   (Fig. 9d), nitrate concentration average is 7.2 ± 1.06 μmol kg^{-1}. High values (> 6.5 μmol kg^{-1}) are found

454   in the westernmost regions (Alboran Sea, Algerian Sea, Gulf of Lion, Balearic Sea and the Liguro-

455   Provençal Basin), while the easternmost regions (Tyrrhenian Sea, Sicily Channel), exhibit much lower

456   concentrations (between 4.5 and 6.5 μmol kg^{-1}).

457   Similar features are observed in the deep layer, at 1500 m (Fig. 9a), with nitrate concentrations

458   increasing all over the basin, reaching on average 7.8 - 7.9 μmol kg^{-1} between 1000 and 1500 m depth

459   (Fig. 10a).

460   In both layers (300 m and 1500 m), the difference between the eastern opening of the basin (Sicily

461   Channel) and the western side (Alboran Sea) is noticeable: the Sicily Channel and the Tyrrhenian Sea

462   are under the direct influence of the water masses coming from the oligotrophic EMED, which then

463   gradually become enriched with nutrients along its path, as found by Schroeder et al. (2020).

464   Phosphate concentrations at intermediate depth (see 300 m, Fig. 9e), varied between 0.12 and 0.44 μmol

465   kg^{-1}, and the horizontal map shows the same gradual decrease towards east, with the highest

466   concentrations in the westernmost regions and minimum values in the eastern regions (< 0.25 μmol kg^{-1}

467   ).

468   The average vertical profile over the entire region (Fig. 10b), reveals a maximum in phosphate

469   concentrations between 300 and 800 m depth, related to an increased remineralization process.

470   In the deep layer (see 1500 m, Fig. 9h), phosphate concentration average is 0.36 ± 0.02 μmol kg^{-1}.

471   Generally, the deep layer is homogeneous (Fig. 10b). The difference observed between westernmost

472   regions and the Tyrrhenian Sea remains, though the latter demonstrate higher phosphate concentrations

473   (~ 0.3 μmol kg^{-1}). This variation could be due to the difference in the water masses. The IW inflow from

474   the EMED brings relatively young waters that are depleted in nutrients, while the higher concentrations

475   in the deep layer are signatures of the older resident DW of the Tyrrhenian Sea. The change in the

476   biological uptake in the intermediate source water could explain the regional variability of nutrients.

477   The low productivity (D'Ortenzio and Ribera d'Alcalà, 2009) and the pronounced oligotrophic regime

478   of EMED water (Lazzari et al., 2016) may justify the increase in nutrients in the IW.

479   Silicate concentration distribution at intermediate (300 m, Fig. 9f) and deep layers (1500 m, Fig. 9i),

480   were as expected, showing a notable increase, compared to the surface. Here, the silicate average

481   concentration is 5.83 ± 0.66 μmol kg^{-1}. The maximum values were observed below 800 m, > 8.034 μmol

482   kg^{-1} (Fig. 10c). At 1500 m, silicate distribution is homogeneous all over the basin (on average $8.35 \pm$

483   0.39).

484   Generally, primary producers do not require silicate for their growth as much as they need nitrate and

485   phosphate which explain the disparity between nutrients patterns. Furthermore, at intermediate levels,

the water is warmer than at deep levels, enhancing the dissolution rate and the progressive increase in silicate (DeMaster, 2002). The biogenic silicate is exported to greater depths and continues to dissolve generating inorganic silicate as it sinks to the bottom. The recycling of silicate within the deep-sea sediments is later on redistributed by the deep currents which explain the homogenous horizontal distribution over the entire basin.

Comparing the three nutrients at the same depth levels, at the surface (100 m), it appears that they all show local surface maximum, depending on local events such as strong winds, local river discharge and vertical mixing (Ludwig et al., 2010).

In the easternmost areas, the surface depletion in nutrients (Van Cappellen et al., 2014) is attributed to the variation in the thermohaline properties that has impacted primary production (Ozer et al., 2017) and the export of organic matter to intermediate and deep layers leading to the accumulation of nutrients in these depth ranges.

The Tyrrhenian Sea is not directly connected to convection regions. Here, the EMED water inflow plays a major role. Li and Tanhua (2020) found an increased ventilation of the intermediate and deep layers during 2001 to 2018 in the Sicily channel and a constant AOU between 2001-2016, suggesting a constant ventilation that explains the peculiar nutrient distribution in that area. In the western side of the WMED, intermediate and deep layers exhibit an increase in nutrients. Schroeder et al. (2020) explained this increase in nitrate and phosphate at the intermediate layer with the increase of the remineralization rate at these depths along the path of IW.

The deficiency of inorganic nutrients is explained by the effect of the anti-estuarine circulation, with the IW coming from the EMED, which is known to be poor in nutrients (Krom et al., 2014; Schroeder et al., 2020), accumulates nutrients along its path. Thus, this relative nutrient-rich Mediterranean outflow is lost to the Atlantic Ocean.

Overall, in surface layer, circulation, physical processes, and vertical mixing increase nutrient input while the biological pump controls the decrease.

In the deep layer, the variability is lower (standard deviation is reduced toward the bottom for all three nutrients, see Fig.10), the deep layer accumulates dissolved organic nutrients. In the WMED, the deep layer constitutes a reservoir of inorganic nutrients.
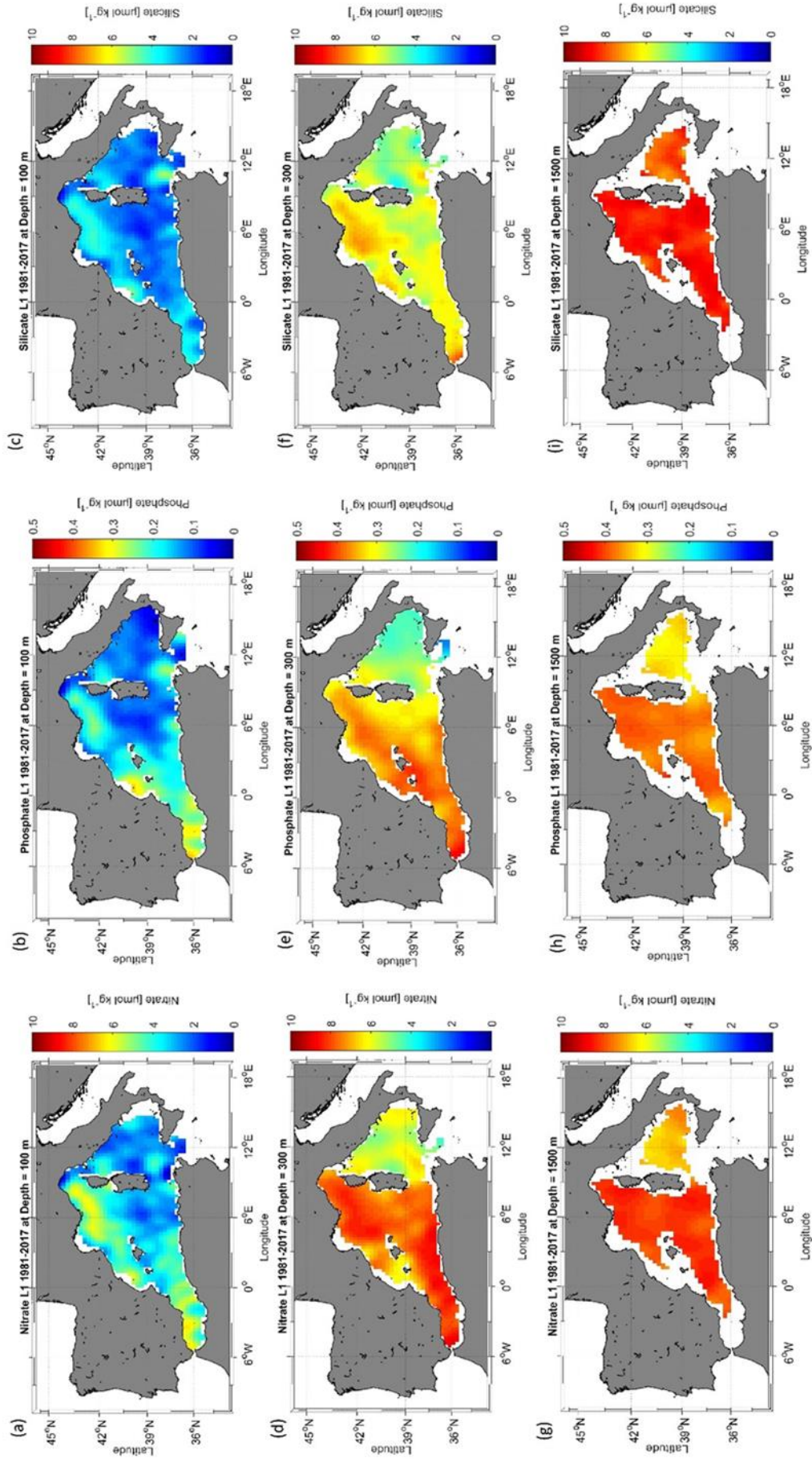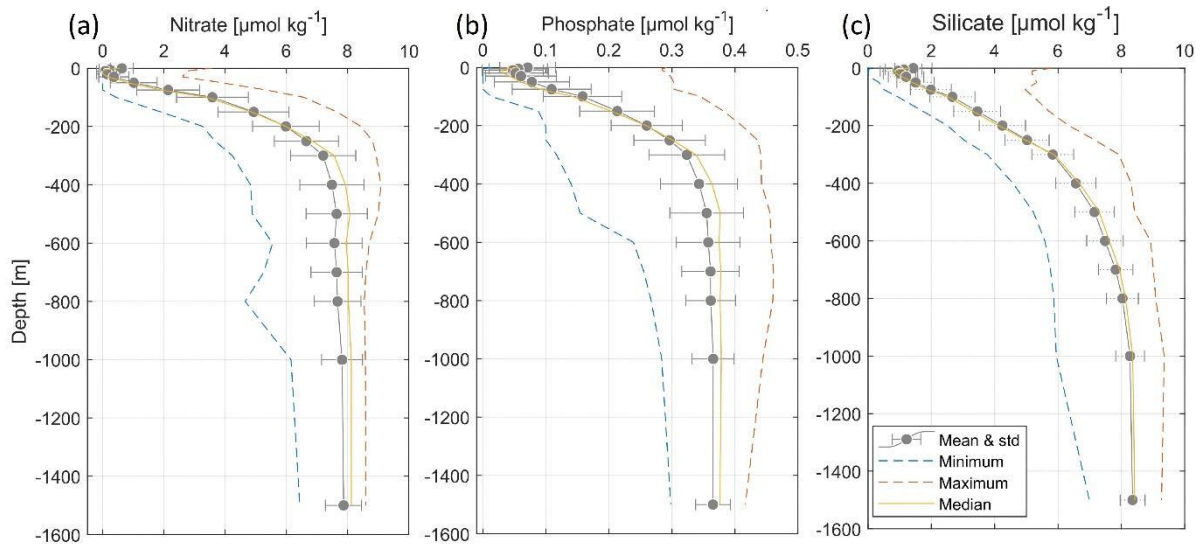
Figure 9. Climatological map distribution of nitrate (a. at 100 m, d. at 300 m, g. at 1500 m) and silicate (a. at 100 m, d. at 300 m, g. at 1500 m), phosphate (a. at 100 m, d. at 300 m, g. at 1500 m) and silicate (a. at 100 m, d. at 300 m, g. at 1500 m) for the period from 1981 to 2017.

Figure 10. Climatological mean vertical profiles of (a) nitrate, (b) phosphate and (c) silicate concentrations in the WMED (1981-2017). Dashed blue line indicates the minimum, dashed orange line indicates the maximum, continuous yellow line indicates median profile, error bars and mean profile are in grey.

4.2 Error fields

The determination of the error field is important to gain insight in the confidence in the climatological results. Mostly, the error estimate depends on the spatial distribution of the observations and the measurement noise. In DIVAnd, there are different methods available to estimate the relative error associated with the analysis fields.

A climatological field is computed at several depths (19 levels in this case), for different parameters (nitrate, phosphate, and silicate in this case). Given these premises and following the approach of similar climatologies (GLODAPv2.2016b, Lauvset et al., 2016; SeaDataNet aggregated data sets products, Simoncelli et al., 2015), for the BCG-WMED the error fields were estimated using the default DIVAnd method, i.e. the "clever poor man's error approach", a less time consuming but efficient computational approach. According to Beckers et al. (2014) who also provides details about the mathematical background of the error fields computation, this method appropriately represents the true error and provides a qualitative distribution of the error estimate. This estimate is used to generate a mask over the analysis fields. Two error thresholds were applied (0.3 (L1) and 0.5 (L2)). Fig.8b., show the main error that occurs in regions void from measurements. An example of the analysis masked with the error thresholds output is shown in Fig.8c (L1) and Fig.8d (L2). The associated error fields with the analysis fields are integrated in the data product.

4.3 Comparison with other biogeochemical data products

In this section, a comparison of the BGC-WMED product with the most known global and/or regional climatologies, that are frequently used as reference products for initializing numerical models, is made.

Specifically, the analyzed fields are compared to the reference data products WOA18 (Garcia et al., 2019), a large scale illustration of nutrient distribution computed by objective analysis using the World Ocean Database 2018 (Boyer et al., 2018). The new product is also compared to the reanalysis of the Mediterranean Sea biogeochemistry, medBFM, a CMEMS product that assimilates satellite and Argo data and includes terrestrial inputs of nitrate and phosphate from 39 rivers (Teruzzi et al., 2019).

Since the products used for inter-comparison were not originated from the same interpolation method, not for the same time period and with different spatial resolution, here the comparison is mostly targeted on the general patterns of nutrients in the region.

Comparisons are carried out between horizontal maps (Fig.11-12-13), as well as along a vertical longitudinal transect (Fig.16-17-18). In addition, following Reale et al. (2020), the first 150 m have been evaluated (Fig.14-15), since this is a depth level with a representative amount of in situ observations in all three products. The evaluation is based on the estimation of horizontal average, on BGC-WMED climatology, the medBFM biogeochemical reanalysis and the WOA18 climatology by subregion. i.e. a spatial subdivision made according to Manca et al. (2004).

Products have a different grid resolution, thus to compare them and combine variables on a compatible grid, the BGC-WMED new climatological data product (at $0.25° \times 0.25°$) for the periods 1981-2017, 2005- 2017 and the medBFM biogeochemical reanalysis (at $0.063° \times 0.063°$) (Teruzzi et al. 2019) (https://doi.org/10.25423/MEDSEA_REANALYSIS_BIO_006_008) for the period 2005- 2017, are regridded on the WOA18 ($1° \times 1°$) grid , changing the resolution, of the existing grid to facilitate the comparison of the transect from each product.

The regridding is computed at all depth levels of the different products using nearest neighbor interpolation. Prior to the interpolation, the medBFM reanalysis of nitrate and phosphate have been averaged across the period 2005-2017.

We then calculated spatial maps of the mean difference at 150 m between the new climatology and the reference products and then an average across subregions was performed.

4.3.1 Comparison with WOA18 at 150 m

Fig. 11-12-13 show the analysis at the 150 m depth surface for the three nutrients. The BGC-WMED (1981-2017) product reveals detailed aspects of the general features of nitrate (Fig. 11.a), phosphate (Fig. 12a) and silicate (Fig.13a).

23

568　　For the three nutrients, the new product reproduces patterns similar to the WOA18 all over the region.

569　　It shows well-defined fields and higher values of nitrate and phosphate concentrations. In the new

570　　product, nitrate concentrations varied between 2.31 -7.3 μmol kg^{-1} the WOA18 values were 2.19 - 5.99

571　　μmol kg^{-1}.Phosphate ranges were similar between the two products between (0.092- 0.35 μmol kg^{-1}

572　　(BGC-WMED) and 0.095 - 0.35 μmol kg^{-1} (WOA18)). Likewise, Silicate range values at 150 m were

573　　not different (2.07 - 4.99 (BGC-WMED) and 1.57 - 5.75 μmol kg^{-1}(WOA18)).

574　　The average RMS difference (RMSD) calculated from the difference between the WOA18 and BGC-

575　　WMED all over the region at 150 m is about 1.14 μmol kg^{-1} nitrate (Fig. 11c), 0.055 μmol kg^{-1} for

576　　phosphate (Fig. 12c) and 0.91 μmol kg^{-1} for silicate (Fig. 13c). Overall, the RMS error values were low

577　　indicating limited disparity between the two products.

578　　The difference field for every grid point reflects this discrepancy and shows areas with limited

579　　agreement between the two products that can have a difference >2 μmol kg^{-1} for nitrate (Fig. 11c), >0.1

580　　μmol kg^{-1}for phosphate (Fig. 12c), >1.5 μmol kg^{-1}for silicate (Fig. 13c). This dissimilarity is also noted

581　　with the low r^2 (Fig. 14) (0.34, 0.20, 0.095 for nitrate, phosphate, and silicate respectively)

582　　The distribution of the surface nitrate concentrations (at 150 m) (Fig. 11a) of the new product is similar

583　　to that shown in WOA18 (Fig. 11b). The largest difference between the two products occurs in northwest

584　　areas and in the Alboran Sea (Fig. 11c), areas of higher concentrations, a more nutrient rich surface

585　　water as described in section 4.1. The difference is pronounced in these regions likely because of the

586　　occurrence of upwellings along the African coast and seasonal vertical mixing in the northern WMED,

587　　contributing to the upload of nutrients to the surface which could explain the high nitrate and phosphate

588　　concentration in the BGC-WMED. The WOA18 maps show weaker values of nutrient concentrations

589　　compared to the new product which does not mean that there are fewer physical drivers, but it might

590　　indicate that the new product holds more in situ observations than the WOA18 in the WMED.

591　　Phosphate surface concentrations (Fig. 12) show similar differences as nitrate. The largest difference

592　　with the surface phosphate of the WOA18 is found in the Alboran Sea, Northern WMED and Sicily

593　　region (Fig. 12c).

594　　As for silicate, the surface distribution shows large differences (Fig. 13c). The highest values are

595　　observed in the northwest area of the new product, and in the Alboran Sea in the WOA18 climatology ,

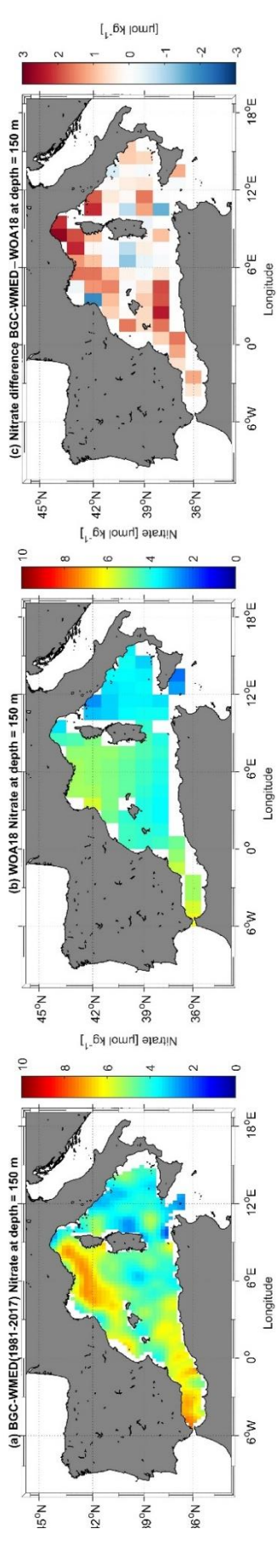596　　this again accounts for the data coverage difference.

Figure 11. (a) BGC-WMED (1981-2017) Nitrate climatological field at 150 m depth; (b) WOA18 nitrate climatological field at 150 m depth; (c) difference between BGC-WMED and WOA18 nitrate fields at 150 m .
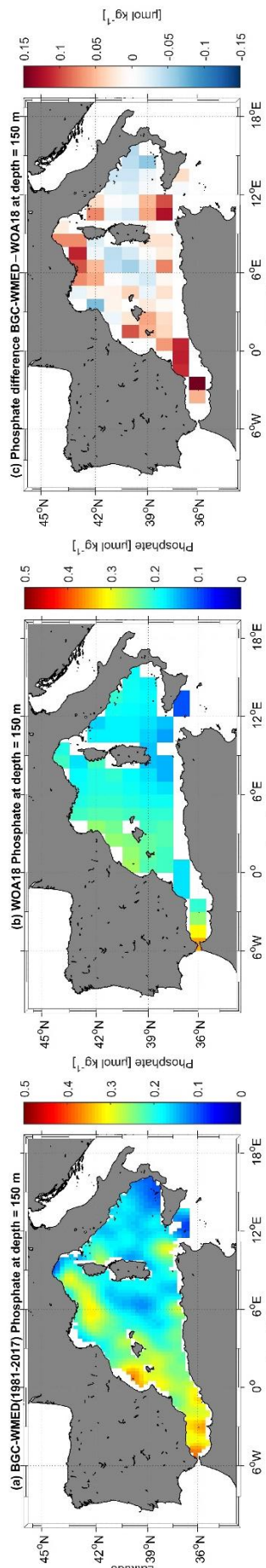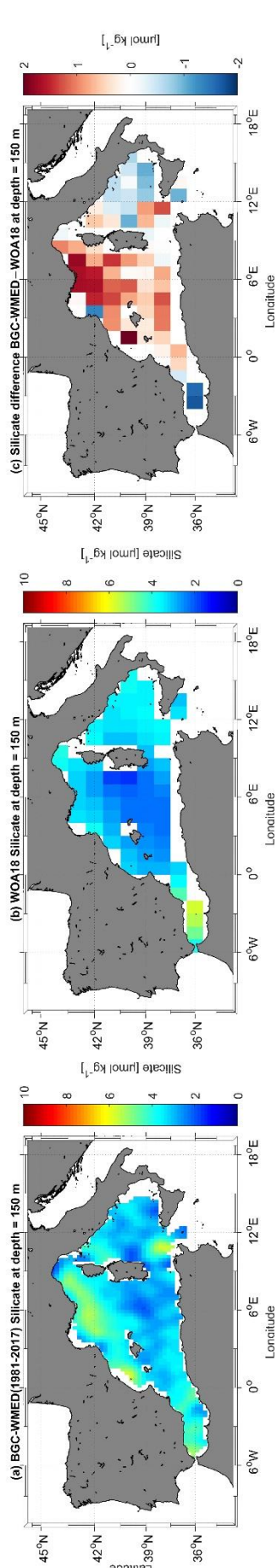

Figure 12. The same as Fig. 11 but for Phosphate.
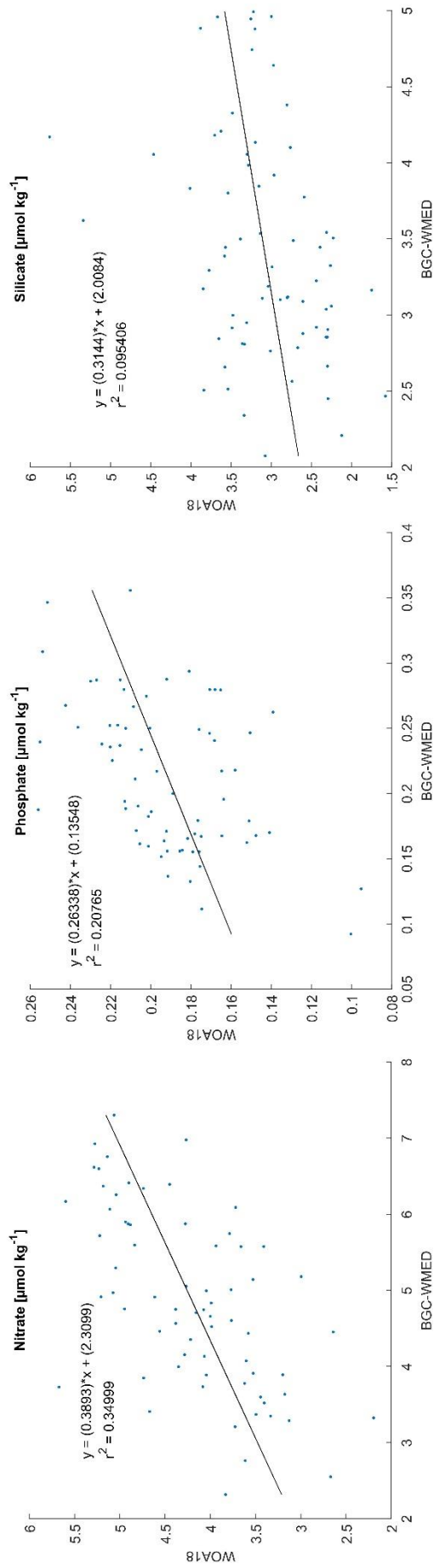

Figure 13. The same as Fig. 11 but for Silicate.

Figure 14. Scatterplot showing the WOA18 data as a function of the BCG-WMED climatology at 150 m with the regression line.

597

598   4.3.2 Regional horizontal comparison above 150 m average nutrient concentrations

599   The inorganic nutrient mean concentrations resulting from the climatology of this work (period 2005-
600   2017), and from both the medBFM reanalysis product and the WOA18 are compared in the upper layer
601   of 12 subregions of the WMED (in Table 4 and Fig. 15).

602   Results show a general agreement between BGC-WMED and the other two products in some
603   subregions, nonetheless, there are some differences as shown in section 4.3.1.

604   Upper layer nitrate average concentrations (Fig. 15a) are decreasing eastward, from the Alboran Sea
605   (DS1) to the Algerian basin (DS3, DS4) and the Balearic Sea (DS2). The western part of the basin is an
606   area under the direct influence of the inflowing Atlantic surface waters, where nitrate is known to be
607   present in excess compared to phosphate probably due to atmospheric N_2 input (Lucea et al., 2003). In
608   the DS1, BGC-WMED nitrate levels are lower than the WOA18 nitrate levels while in DS3, DS2 and
609   DS4 the average nitrate concentrations are similar to the WOA18.

610   From the Algerian basin (DS4, DF1) to Liguro-Provençal (DF3) regions, there is an increase in the
611   average nitrate in all products, this is the south-north gradient. Some difference arises, where the new
612   product is lower than the WOA18.

613   In the eastern regions, the lowest average concentrations of the WMED are found. Here, the difference
614   between products is smaller, with medBFM reanalysis being lower than the new product and the
615   WOA18.

616   As for phosphate (Fig. 15b), known to be the limiting nutrient of the WMED, because it is rapidly
617   consumed by phytoplankton (Lucea et al., 2003), its average levels are low in DS1, DS3, DS2 and DS4,
618   in WOA18, medBFM reanalysis and BGC-WMED. The latter did not agree well with the other products
619   in DS2, where it was slightly higher. Phosphate average concentrations slightly increase in DF1, DF2
620   and DF3 in all three products. The increase is explained by the vertical mixing process occurring in the
621   northern WMED.

622   Upper surface phosphate concentrations average start to decrease progressively through the Ligurian
623   East (DF4), Tyrrhenian Sea (DT1, DT3), Sardinia Channel (DI1) and Sicily Channel (DI3).The BGC-
624   WMED was in agreement with medBFM reanalysis in those subregions aside from concentrations in
625   DI3, where the new product showed higher levels.

626   The BGC-WMED climatology shows reasonable agreement in the upper average concentrations of
627   nitrate and phosphate that are similar in order of magnitude to the other products (Fig. 15). The
628   difference with the WOA18 resides in the wider temporal window of the observation (starting from

27

629   1955). The new climatology in some subregions has a better spatial coverage of in situ observation than

630   the WOA18 (Garcia et al., 2019) and the medBFM reanalysis (Teruzzi et al., 2019).

631   On the other hand, the average silicate (Fig. 15c) of the new product and the WOA18 varied between

632   regions. Significant difference is found between the two products in DS2, DS4, DF1, DF2, DT1, DT3,

633   DI1 and DI3, while in DS1, DS3 and DF4 mean silicate is consistent between the two products.

634   Overall, the three products show strongly similar features between regions (similar curve shape).
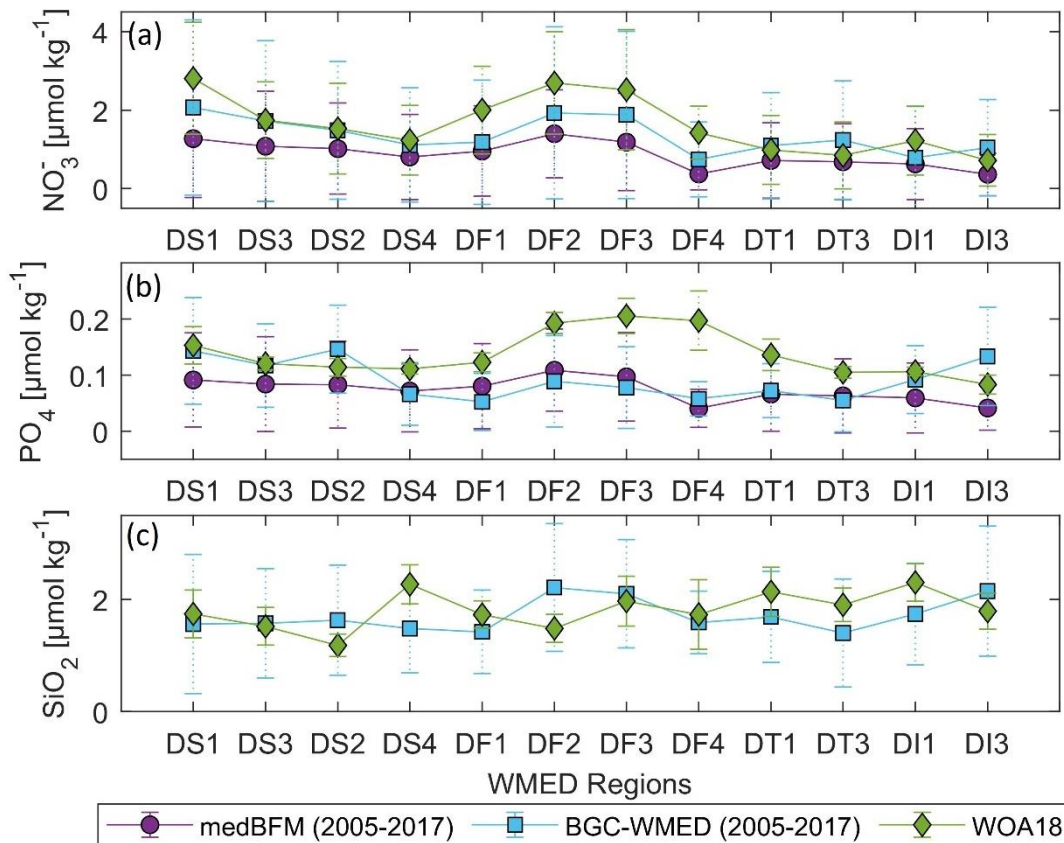
636   **Figure 15.** Nutrient average concentrations and standard deviation comparison in the upper 150 m

637   (values in Table 4).

638

639

640

641

642

643

644

645

647 **Table 4.** Nutrient average concentrations and standard deviation in the upper 150 m. All products were

648 interpolated on 1° grid resolution (see Figure S2 (Belgacem et al., 2020)).

Subregion/ Coverage	Data product	Nitrate	Phosphate	Silicate
DS1- Alboran Sea (35°N– 37.3°N, -6°E– -1°E)	medBFM	1.27(±1.4)	0.09(±0.08)	-
	BGC-WMED	2.06(±2.2)	0.14(±0.09)	1.56(±1.2)
	WOA18	2.81(±1.4)	0.15(±0.03)	1.74(±0.4)
DS3- Algerian West (35.36°N– 38.3°N, -1°E– 4.3°E)	medBFM	1.07(±1.4)	0.08(±0.08)	-
	BGC-WMED	1.72(±2.05)	0.11(±0.07)	1.57(±0.9)
	WOA18	1.74(±0.9)	0.12(±0.01)	1.52(±0.3)
DS2- Balearic Sea (38.3°N– 42°N, -1°E–4.3 °E)	medBFM	1.02(±1.1)	0.08(±0.07)	-
	BGC-WMED	1.48(±1.7)	0.14(±0.07)	1.63(±0.9)
	WOA18	1.53(±1.1)	0.11(±0.01)	1.18(±0.2)
DS4- Algerian East (36.3°N– 39.18°N, 4.3°E– 8.24°E)	medBFM	0.80(±1.08)	0.07(±0.07)	-
	BGC-WMED	1.11(±1.4)	0.06(±0.05)	1.48(±0.7)
	WOA18	1.23(±0.8)	0.11(±0.009)	2.27(±0.3)
DF1- Algero-Provençal (39.18°N– 41°N, 4.3°E– 9.18°E)	medBFM	0.96(±1.15)	0.08(±0.07)	-
	BGC-WMED	1.18(±1.5)	0.05(±0.05)	1.42(±0.7)
	WOA18	2.00(±1.1)	0.12(±0.01)	1.73(±0.2)
DF2- Gulf of Lion (42°N–43.36°N, 1°E–6.18°E)	medBFM	1.39(±1.19)	0.10(±0.07)	-
	BGC-WMED	1.92(±2.1)	0.08(±0.08)	2.21(±1.1)
	WOA18	2.68(±1.3)	0.19(±0.01)	1.48(±0.2)
DF3- Liguro-Provençal (41°N– 45°N, 6.18°E– 9.18°E)	medBFM	1.18(±1.2)	0.09(±0.07)	-
	BGC-WMED	1.88(±2.1)	0.07(±0.07)	2.10(±0.9)
	WOA18	2.52(±1.5)	0.20(±0.03)	1.97(±0.4)
DF4- Ligurian East (42.48°N–45°N, 9.18°E– 11°E)	medBFM	0.37(±0.4)	0.04(±0.03)	-
	BGC-WMED	0.74(±0.9)	0.05(±0.03)	1.59(±0.5)
	WOA18	1.42(±0.6)	0.19(±0.05)	1.73(±0.6)
DT1- Tyrrhenian North (39.18°N–42.48°N, 9.18°E– 16.16°E)	medBFM	0.71(±0.9)	0.06(±0.06)	-
	BGC-WMED	1.09(±1.3)	0.07(±0.04)	1.69(±0.8)
	WOA18	0.98(±0.8)	0.13(±0.02)	2.13(±0.4)
DT3- Tyrrhenian South (38°N– 39.18°N, 10°E– 16.16°E)	medBFM	0.68(±0.96)	0.06(±0.06)	-
	BGC-WMED	1.23(±1.5)	0.05(±0.05)	1.40(±0.9)
	WOA18	0.84(±0.8)	0.10(±0.01)	1.90(±0.2)
DI1- Sardinia Channel (36°N– 39.18°N, 8.24°E– 10°E)	medBFM	0.62(±0.9)	0.05(±0.06)	-
	BGC-WMED	0.78(±1.3)	0.09(±0.06)	1.74(±0.9)
	WOA18	1.22(±0.8)	0.10(±0.007)	2.3(±0.30)
DI3- Sicily Channel (35°N– 38°N, 10°E–15°E)	medBFM	0.36(±0.5)	0.04(±0.03)	-
	BGC-WMED	1.04(±1.2)	0.13(±0.08)	2.15(±1.1)
	WOA18	0.72(±0.6)	0.08(±0.01)	1.79(±0.3)

649 4.3.3 Regional vertical comparison of nitrate and phosphate concentrations

650 As the last step in the comparison between the different products, it is investigated how the new

651 climatology represents the vertical distribution by comparing the new climatological values for the

652 period 2005-2017 with the medBFM reanalysis and the WOA18.

653   We extracted data values along a longitudinal transect across the Algerian basin in the west-east

654   direction (Fig. 16). The transect was selected according to previous studies (D'Ortenzio and Ribera

655   d'Alcalà, 2009; Lazzari et al., 2012; Reale et al., 2020) and since the Easternmost part of the domain is

656   showing markedly features, a transect across the Tyrrhenian Sea is extracted as well (Fig. 16). Silicate

657   is not included as it was not represented in the medBFM model.

658   Vertical sections of nitrate and phosphate in the Algerian Sea show a common agreement between

659   products about the main patterns found along the water column, i.e. the nutrient depleted surface layer

660   and the gradual increase toward intermediate depths, we note as well the west to east decreasing gradient

661   in the three products, yet, there are some inequalities.

662   Below 100 m, there is a significant difference between products and a poor qualitative agreement.

663   Nitrate distribution is dominated by the nutrient enriched IW, with high values ($>7\,\mu$mol kg^{-1}) increasing

664   from east to west (Fig. 16). Phosphate shows similar patterns in the surface layer, exhibiting very low

665   concentration and a progressive increase down to 300 m ($> 0.35\,\mu$mol kg^{-1}) noted also in the WOA18.

666   The reanalysis showed a more smoothed field, below 100-300 m, with phosphate concentration between

667   0.20 and 0.30 μmol kg^{-1}. The highest values for phosphate were found below 250 m from 0°E to 3°E in

668   the new product. The BCG-WMED transect defines very well the different depth layers, the upper

669   intermediate layer is rich with nutrient concentration with $> 8\,\mu$mol kg^{-1} for nitrate (BGC-WMED) and

670    $>0.35\,\mu$mol kg^{-1} for phosphate (BGC-WMED and WOA18).

671   The vertical section along the Tyrrhenian Sea (Fig. 16) also shows a decrease from west to east in nitrate

672   concentrations. The same gradient is found also in phosphate in agreement with nutrient distribution

673   shown from the WOA18. From the section of the medBFM reanalysis, it is not easy to identify the west-

674   east gradient that we mentioned before. It could be suggested that the model under-estimate the vertical

675   features in the Eastern (Tyrrhenian Sea: 100-300 m, nitrate vary between 1.4 and 4.2 μmol kg^{-1},

676   phosphate between 0.13 and 0.20 μmol kg^{-1}) and western part (Algerian basin: 100-300 m, nitrate vary

677   between 2.1 and 5.4 μmol kg^{-1}, phosphate between 0.15 and 0.255 μmol kg^{-1}). These values are lower

678   than the ones found in the BGC-WMED (Tyrrhenian Sea: 100-300 m, nitrate range between 3 to 6 μmol

679   kg^{-1}, as for phosphate values oscillate between 0.10-0.27 μmol kg^{-1};Algerian basin: 100-300 m, nitrate

680   range between 3.6 to 8 μmol kg^{-1}, as for phosphate values oscillate between 0.18-0.36 μmol kg^{-1}).

681   While the WOA18 reproduces similar patterns as the new climatology (Tyrrhenian Sea: 100-300 m,

682   nitrate vary between 1.8 and 5.7 μmol kg^{-1}, phosphate between 0.33 and 0.20 μmol kg^{-1}) and western

683   part (Algerian basin: 100-300 m, nitrate vary between 2.8 and 6.8 μmol kg^{-1}, phosphate between 0.16

684   and 0.34 μmol kg^{-1}).

685   The products illustrate the nutrient-poor water in the eastern side (Tyrrhenian Sea) and the relatively

686   nutrient-rich water found in the western transect (Algerian basin).

687 The BGC-WMED product captures details in Fig. 16 about the longitudinal gradient in nitrate and
688 phosphate, along the water column where nutrient sink deeper from west to east as previously seen in
689 Pujo-Pay et al. (2011) and Krom et al. (2014), an increased oligotrophy from west to east with higher
690 concentrations in the two nutrients in the western side of the section and a more oligotrophic character
691 toward east.

692 The differences between products could be explained by the difference in the data coverage, time span
693 and the difference in methods used to construct the climatological fields.

694 The variability in nitrate and phosphate fields along the transect extracted from the BGC-WMED reflects
695 the high resolution of the product allowing the screening of vertical structure controlling nutrient
696 contents. Based on a visual comparison, the new product is able to reproduce similar patterns as to the
697 WOA18 and to a lesser extent the medBFM reanalysis.

698 Fig. 17 examines the vertical difference of nitrate and phosphate concentration for the BGC-WMED
699 with the medBFM reanalysis along the Algerian basin (Fig.17a, nitrate; Fig.17b, phosphate) and
700 WOA18 (Fig.17c, nitrate; Fig.17d, phosphate).

701 The vertical section shows a strong agreement at the surface for nitrate between the BGC-WMED and
702 the medBFM reanalysis (Fig. 17a), while the vertical difference with WOA18 demonstrates that nitrate
703 values in the new product are lower than the WOA18 at 50- 75 m (Fig. 17c).

704 The difference increases with depth, below 100 m, the BGC-WMED nitrate climatology is higher than
705 the medBFM with a difference ranging between 0.6 and 2.4 μmol kg^{-1}, similar observation is noted in
706 the WOA18 (Fig. 17c). In Fig.17a and Fig.17c, we identify patterns in the vertical structure of nitrate
707 in the eastern portion of the transect.

708 Regarding phosphate, differences between the new climatology and the medBFM reanalysis are noted
709 (Fig. 17b) where the BGC-WMED shows high concentrations in the first 100 m and between 150 m and
710 300 m (differences of 0.02 - 0.08 μmol kg^{-1}), this difference decreases at 100-150 m. At the eastern
711 portion of the transect (6°E to 7.5°E), we find an agreement between the two products.

712 Conversely, the vertical sections of the differences between BGC-WMED and WOA18 in phosphate
713 (Fig.17 d) show similarities, with the new product being lower than the WOA18 in the first 50 m. Large
714 difference is found on both sides of the transect below 100 m, while in the center of the transect, the
715 difference in phosphate is reduced to 0-0.02 μmol kg^{-1}.

716 Fig.18 compares the vertical difference of nitrate and phosphate along the Tyrrhenian Sea transect. In
717 general, the difference transect in the Tyrrhenian Sea shows similar features with medBFM reanalysis
718 and the WOA18 as in Algerian basin. Fig.18d captures the west to east gradient in phosphate. The
719 WOA18 overestimated phosphate in the surface layer.
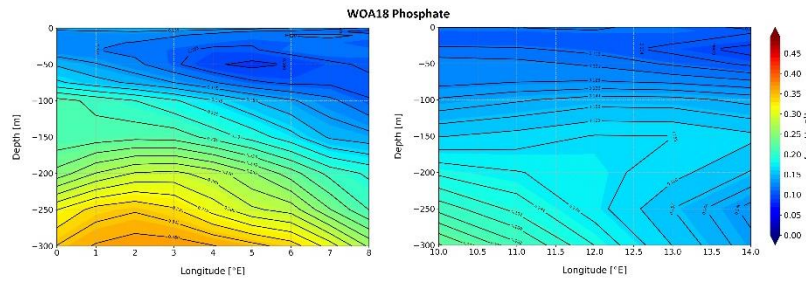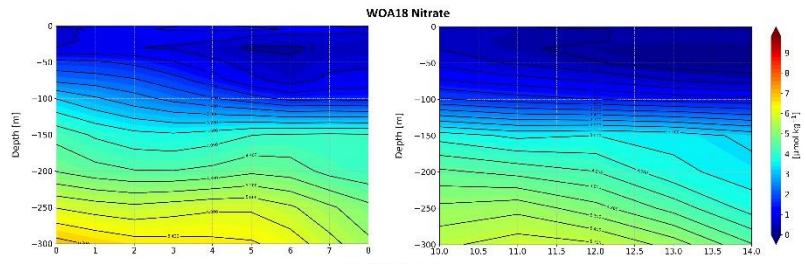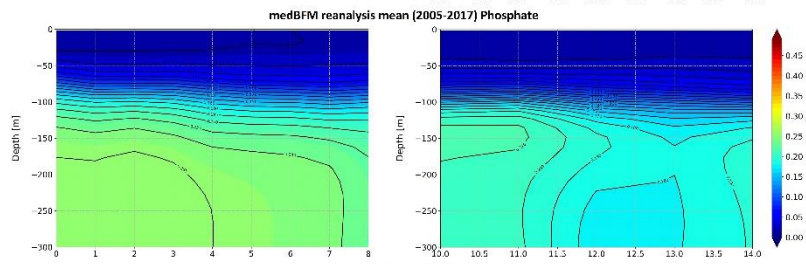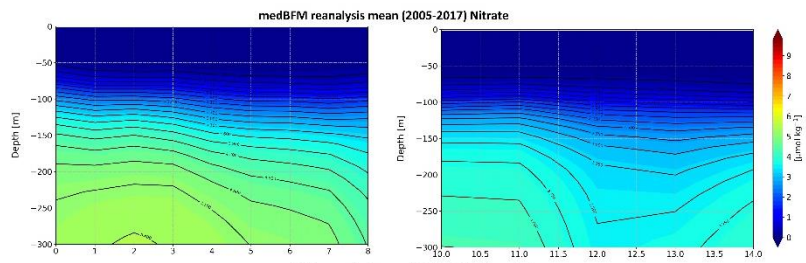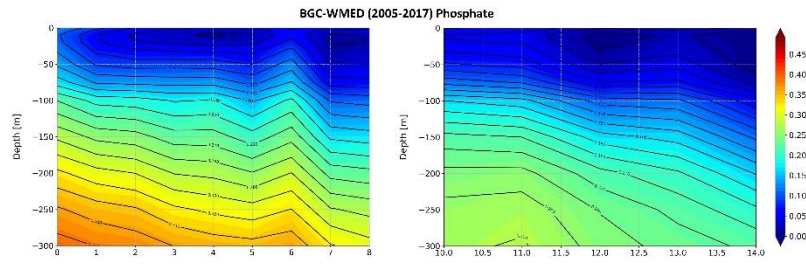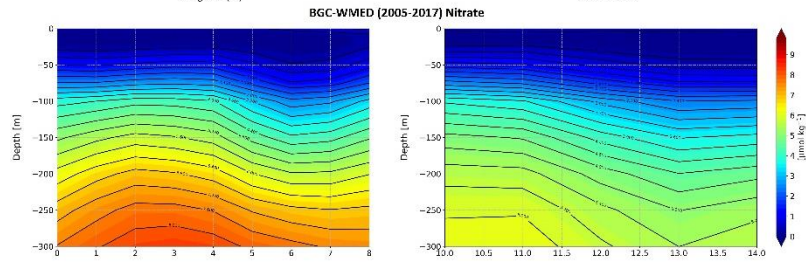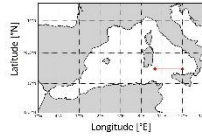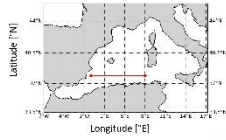
721 **Figure 16.** Vertical distribution of nitrate and phosphate from the Algerian basin and Tyrrhenian Sea.

722 Colors show the gridded values from the three different products: BGC-WMED, medBFM reanalysis

723 (Teruzzi et al., 2019) and the WOA18 (Garcia et al., 2019).

724 Based on the new climatology comparison with the WOA18 and the reanalysis, it is concluded that the

725 new product is consistent with the main features of previous products and show the large-scale patterns

726 and underline well the characteristics of the water mass layers.

727 The study also provides an examination of the nitrate and phosphate distributions along a longitudinal

728 transect across the Algerian Basin (Western WMED) and across the Tyrrhenian Sea (Eastern WMED).

729 We have shown that the western basin is relatively high in nutrients compared to the Eastern basin. The

730 increased oligotrophic gradient from west to east could be attributed to the difference in the

731 hydrodynamic patterns related to the water mass specific properties that are affected by the EMED and

732 the Atlantic ocean inflows, and to the local sources of nutrients (Ribera d'Alcalà et al., 2003; Schroeder

733 et al., 2010). Study of Crispi et al. (2001) inferred the biological activity that is responsible for the

734 oligotrophic gradient.
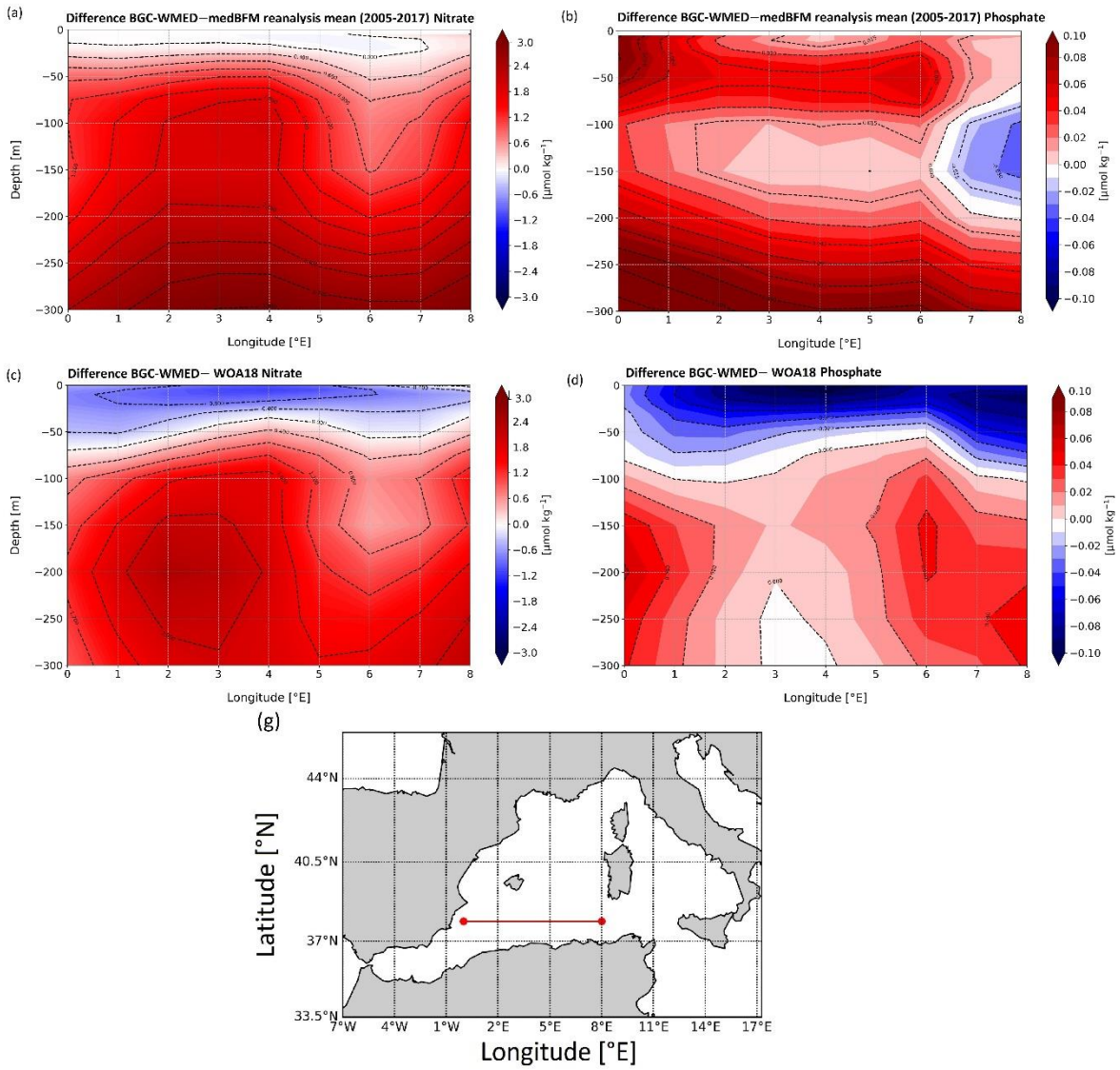
Figure 17. Difference of vertical section from the Algerian basin between BGC-WMED and medBFM
(a. nitrate, b. phosphate), BGC-WMED and WOA18 (c. nitrate, d. phosphate), with dashed contour lines
and labels.
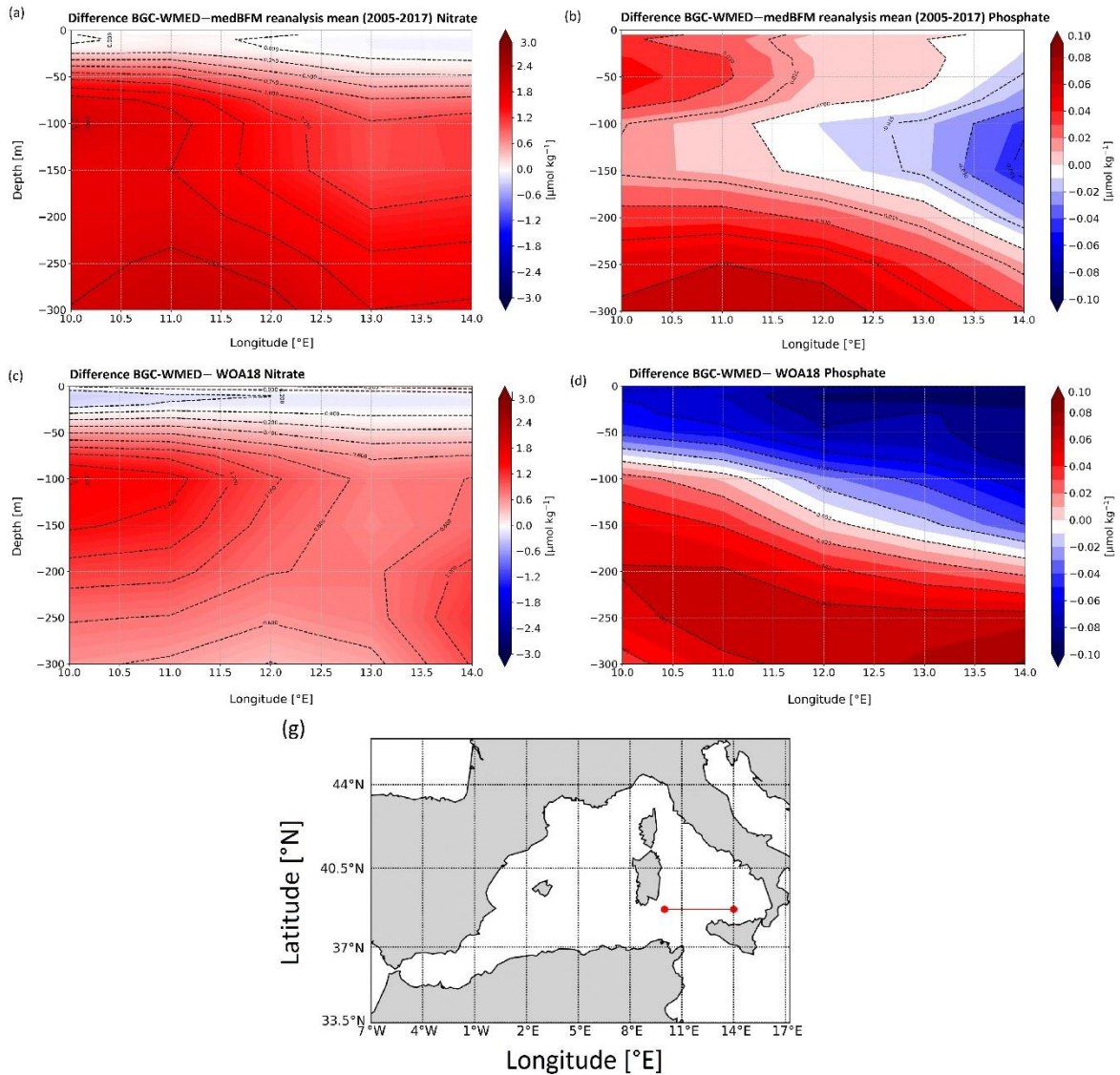
Figure 18. Same as Fig.17 but for the vertical section from the Tyrrhenian Sea.

4.4 Temporal comparison: 1981-2004 vs 2005-2017

In this section, we compare between two climatological periods (1981-2004 vs 2005-2017). The distinction between the two periods was based on the occurrence of the Western Mediterranean Transition (WMT) that started in 2004/05, during which there was a progressive increase in temperature and salinity of the IW that led to important deep convection events, substantially increasing the rate of DW formation between 2004 and 2005 (Schroeder et al., 2016).

The result of this climatological event was that a newly generated DW, denser, saltier, and warmer than the old WMDW, filled up the WMED. The new WMDW propagated east toward the Tyrrhenian Sea and west toward the Alboran Sea and Gibraltar (Schroeder et al., 2016).

A recent study of Li and Tanhua (2020) demonstrated an enhanced ventilation in the WMED deep layers despite the continuous overall increase in temperature (Bindoff et al., 2007), salinity and density of

intermediate and deep layers after the WMT (Schroeder et al., 2016; Vargas-Yáñez, 2017). An increased ventilation means a DW renewal (Schroeder et al., 2016; Tanhua et al., 2013) subsequently a well oxygenated waters, implying an increase in the decomposition of the sinking organic matters into inorganic nutrients, thus causing changes of biogeochemical cycles (Shepherd et al., 2017). What happened in the WMED was not a permanent continuous event, since DW formation faded during the years 2006 and 2007, to restart again in 2008 (Li and Tanhua, 2020). In this section, we investigate the possible impact of WMT on biogeochemical characteristics at different depth levels (with a focus on nitrate, phosphate and silicate regional distribution and patterns).

We considered depth levels that represent the usual three layers: the surface (100 m; Fig.19a,d-20a,d-21a,d), intermediate (300 m; Fig.19b,e- 20b,e- 21b,e) and deep layers (1500 m; Fig.19c,f -20c,f- 21c,f).

The WMED surface layer is dominated by the AW coming through the Alboran Sea, a permanent area of upwelling (García-Martínez et al., 2019), where there is a continuous input of elements from the layer below to the surface (Fig. 19a- 20a- 21a). Nitrate increased after WMT (Fig. 19d- 20d- 21d) by +0.4137 μmol kg^{-1} (Fig. A4a). The largest difference between the two periods reached >+2 μmol kg^{-1} in Sardinia Channel and the Alboran Sea that was explained by the favorable conditions for nitrogen fixation as discussed in Rahav et al. (2013), revealing also that nitrogen fixation rate increased from east-to-west. Phosphate and silicate on the other hand described a decrease at 100 m (Fig. A4a) with about -0.021 and -0.1365 μmol kg^{-1} on average, respectively. Large changes are noticed in the southern Alboran Sea, Sardinia channel and Balearic Sea.

The surface layer exhibits an irregular distribution since it is subjected to seasonal variability. We found an increase in all nutrients at 300 and 1500 m with a maximum identified at intermediate depths in both nitrate and phosphate which is explained by the remineralization of organic matter along the path of the IW. The latter flows westward (from the Levantine to the Atlantic Ocean). Its content in nutrients increases (relatively to the conditions in the EMED) with age (Schroeder et al., 2020). It arrives at the Tyrrhenian Sea, where in Fig.19b-20b-21b (at 300 m depth, 1981-2004), we identify a nutrient-depleted intermediate layer. At this depth level, we observe a gain in the three nutrients after WMT (Fig.19e-20e-21e). On average, the difference between the two periods (pre/post-WMT) for nitrate, phosphate, and silicate, is around +0.8648, +0.0068 and +0.2072 μmol kg^{-1} (Fig. A4b), respectively.

A similar increase after WMT in the deep layer (1500 m), is also found for nutrient concentrations (Fig. 19f, 20f, 21f) in the magnitude of +0.753 for nitrate, +0.025 for phosphate, and +0.867 for silicate (Fig. A4c), which highlights an increase in the downward flow of organic matter remineralization that is supplying the existing pool.

This increase is also illustrated in the climatological mean vertical profile of Fig. 22 in the three nutrients. Nitrate displays a notable vertical difference to the pre-WMT period below 200 m (Fig. 22a). Phosphate difference between the two-time period is larger below 400 m (Fig. 22b). Silicate was different from nitrate and phosphate. It increases progressively with depth (Fig.22c) and demonstrates

788   an enrichment of the DW compared to the 1981-2004 period (Fig. 21c). The maximum values are found

789   in the deep layer, due to the low remineralization rate. With the warming climate, biogenic silica tends

790   to dissolve faster which explains the high concentrations all over the basin even the Tyrrhenian Sea after

791   the WMT.

792   According to Stöven and Tanhua (2014), the impressive volume of the newly formed DW during 2004

793   and 2006, ventilated the old DW decreasing its age, meaning that the WMT could have led to the

794   lowering of the WMED deep layer pool in nutrient as it was pointed out by Schroeder et al. (2010).

795   However, we did not observe this decrease in the climatological analysis after the WMT. It might be

796   due to the temporal variability of the deep convection intensity, since a decrease has been recorded in

797   the Gulf of Lion between 2007 and 2013 (Houpert et al., 2016).

798   A decrease in the deep convection intensity since the WMT (Houpert et al., 2016; Li and Tanhua, 2020),

799   could potentially lead to the reduction in the supply from the nutrient-rich DW (before WMT) to the

800   surface, i.e. the decrease in nutrient could have happened right after the WMT in spring 2005 where

801   Schroeder et al. (2010) reported peculiar divergence between the old WMDW and the new WMDW in

802   nitrate and phosphate; the new WMDW was low in nutrient; later on an intense DW formation event

803   marked the year 2012 with a strong ventilation that has been recorded in the Adriatic Sea that could

804   have affected the WMED. It was not possible to observe this change since we calculated the mean state

805   of the basin spanning a specific period.

806   The spatial distribution of nutrient concentrations after the WMT (2005-2017) was quite different from

807   the one before the WMT (1981-2004). This could also be related to the significant decline in river

808   discharge between 1960 and 2000, which was estimated to 20% (Ludwig et al., 2009). The decrease is

809   also observed in silicate fluxes since silicate loads through river discharge.

810   The change could be explained by the low denitrification rate for nitrate and an increase in the

811   remineralization of organic matter. Ludwig et al. (2009) reported an increase in nitrate and phosphate

812   fluxes that was enhanced by the anthropogenic inputs, loading the deep layer with inorganic nutrients,

813   also it could be associated with the slower ventilation of the WMED waters and a longer residence time.
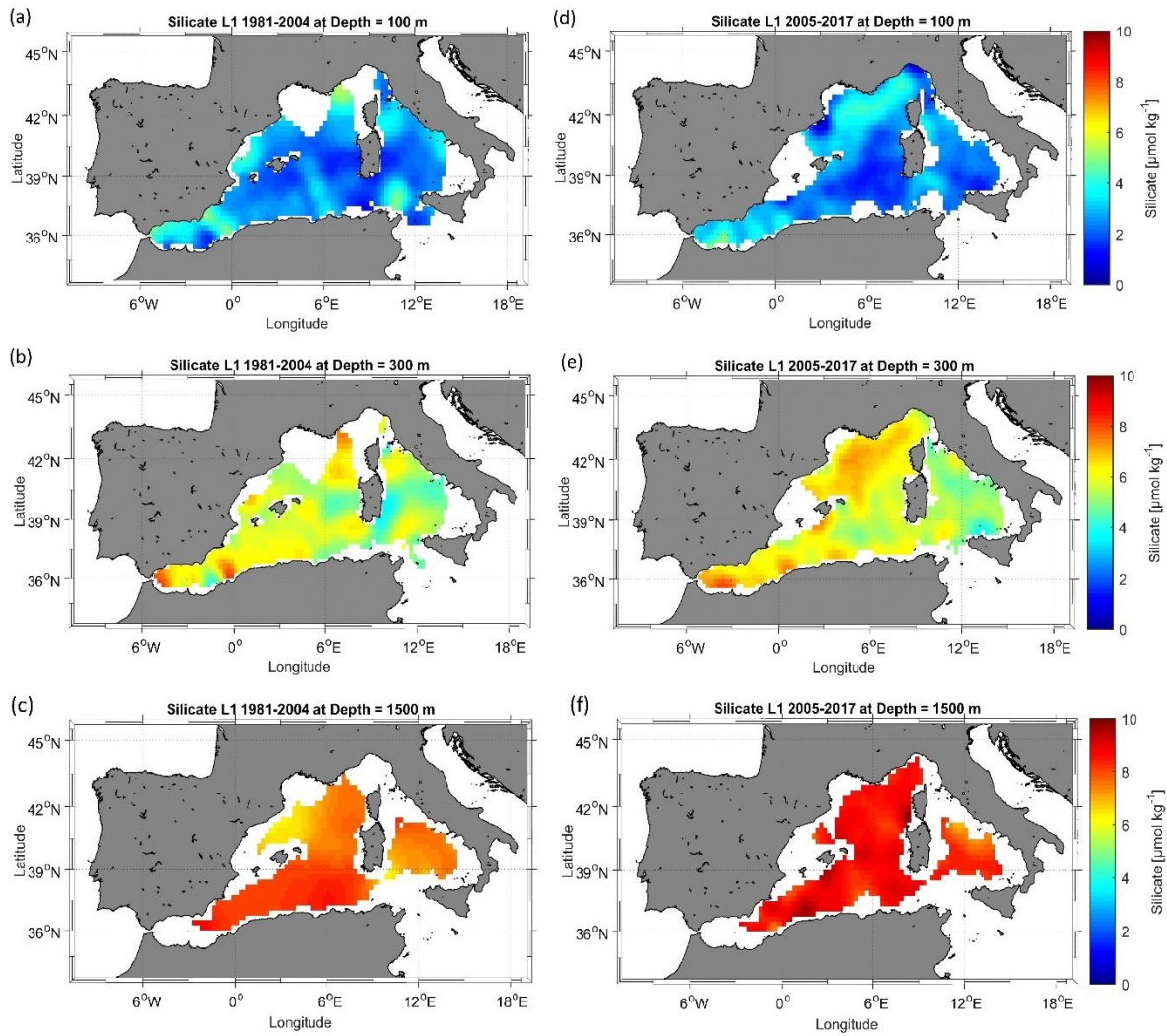
814
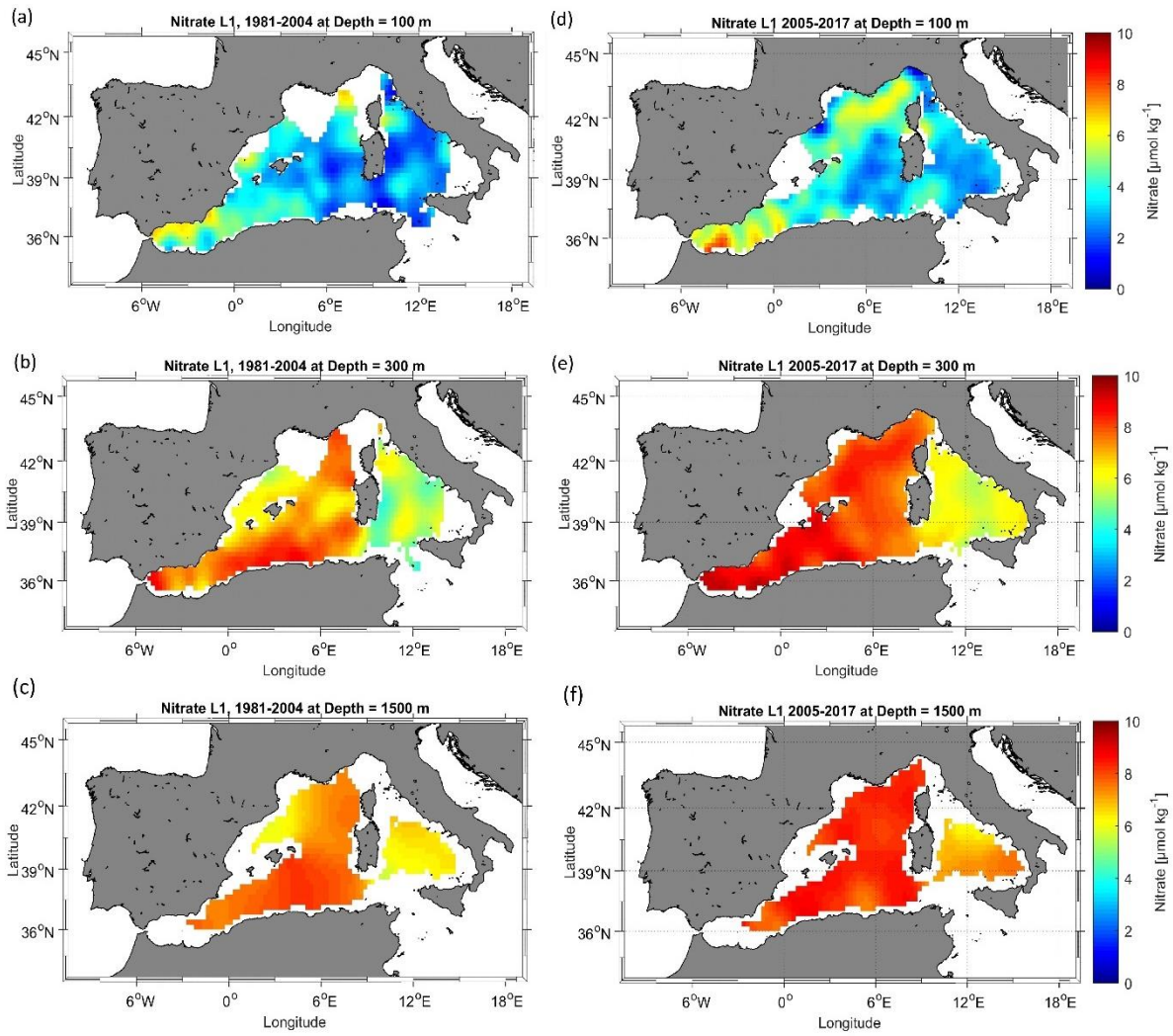
Figure 19. Nitrate climatological field (masked analysis fields masked using relative error threshold = 0.3 (L1)) at 100 m, 300 m, and 1500 m, for two periods: 1981-2004 (a, b, c) and 2005-2017 (d, e, f).
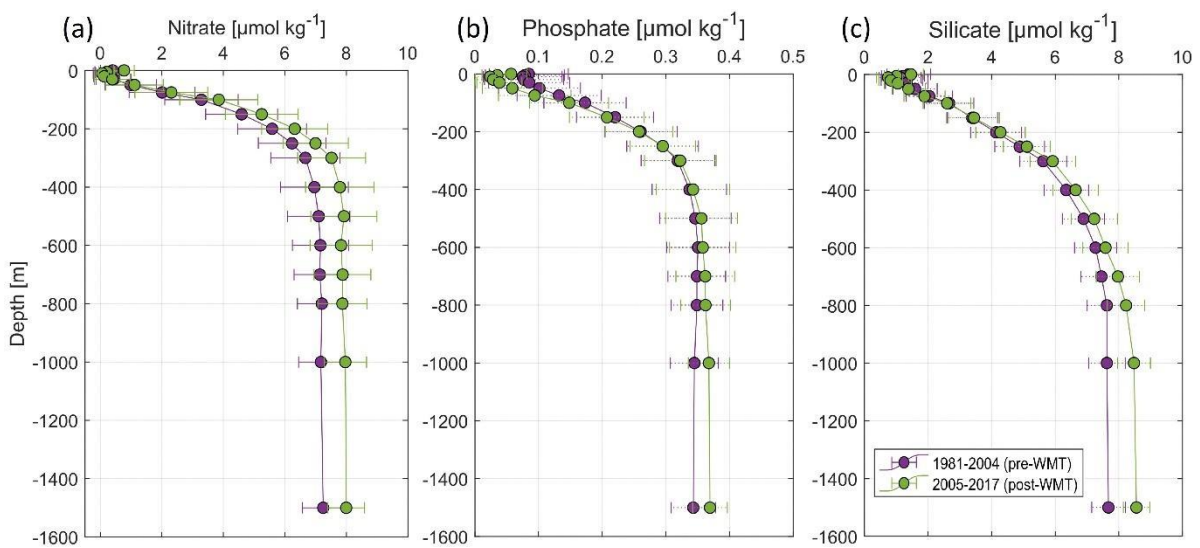
817
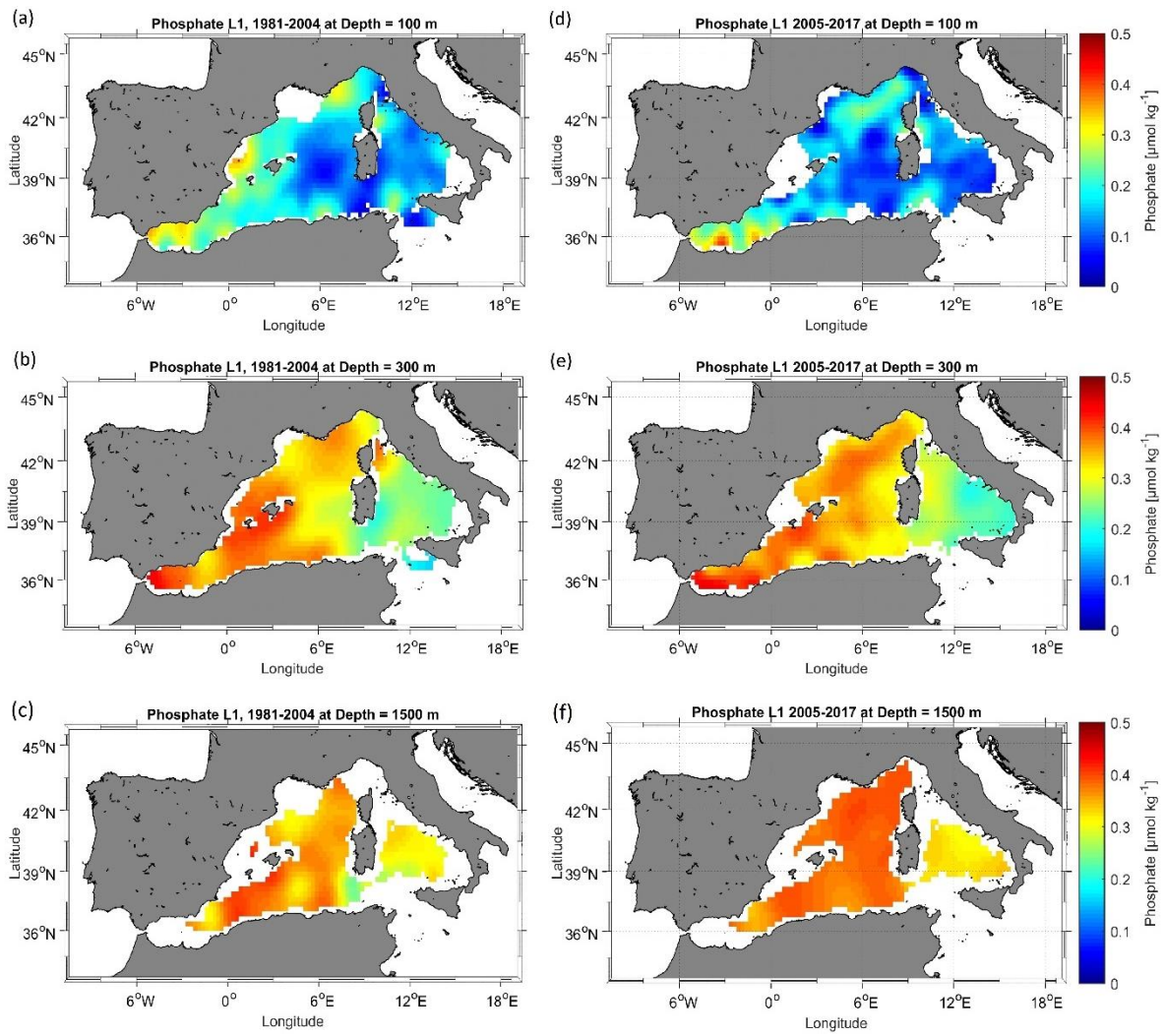
Figure 20. The same as Fig. 19 but for phosphate.

819

820

Figure 21. The same as Fig. 19 but for silicate.

822

Figure 22. Climatological mean vertical profile and standard deviation of (a) nitrate, (b) phosphate and

(c) silicate over the WMED before (1981-2004, in violet) and after WMT (2005-2017, in green).

5 Data availability

The climatologies of Nitrate, Phosphate and Silicate are available as netCDF files from the data repository PANGAEA and can be accessed at https://doi.org/10.1594/PANGAEA.930447 (Belgacem et al., 2021). Ancillary information is in the readme in PANGAEA with the list of variables that are described in table 3 of section 4. The CNR_DIN_WMED_20042017 data are available from PANGAEA (https://doi.org/10.1594/PANGAEA.904172). The MOOSE-GE data are available in the SISMER database (global doi10.18142/235)

6 Conclusion

In this study, we investigated spatial variability of the inorganic nutrients in the WMED and presented a climatological field reconstruction of nitrate, phosphate, and silicate, using an important collection dataset spanning 1981 and 2017. The BGC-WMED new product is generated on 19 vertical levels on a 1/4° spatial resolution grid.

The new product represents very well the spatial patterns about nutrient distribution because of its higher spatial and temporal data coverage compared to the existing climatological products (see Table 1), it is contributing to the understanding of the spatial variability of nutrients in the WMED.

The novelty of the present work is the use of the variational analysis that takes into consideration physical, geographical boundaries, topography, and the resulting estimate of the associated error field.

Comparison with previously reported studies gives that the BGC-WMED reproduces common features and agrees with previous records. The reference products WOA18 and medBFM biogeochemical reanalysis tend to underestimate nutrient distribution in the region with respect to the new product.

The new product captures the strong east-west nutrient gradient and vertical features. The results obtained do not include seasonal or annual analysis fields. However, the aggregated dataset here does show improvements in describing the spatial distribution of inorganic nutrients in the WMED. We acknowledge that computing a climatological mean over a time period is not enough to estimate and detect the climate shift 'WMT' change driven trend. However, comparing climatologies based on the two time periods: 1981-2004 (pre-WMT) and 2005 -2017 (post-WMT) has already produced important results. Notable changes have been found in nutrient distribution after the WMT at various depths.

The results support the tendency to a relative increasing load of inorganic nutrients to the WMED and possibly relate the change in general circulation patterns, changes in deep stratification and warming trends, however, this remains to be evidenced.

The BGC-WMED is a regional climatology that has allowed the identification of a substantial enrichment of the waters, except for the Tyrrhenian Sea where the water column is depleted in nutrients

857 with respect to the western areas of the WMED. The climatology gave information about the spreading

858 of inorganic nutrients inside the WMED at surface, intermediate and deep layers.

859 A future work will suggest a better understanding of the change in nutrients related to water masses

860 associated with ventilation rate, a climatological field along isopycnal surfaces instead of depths and the

861 correlation between potential temperature and nutrients.

Appendix A: Additional information about cruise metadata

862

863 **Table A1.** Summary table of the analytical techniques and instruments used for nutrient analysis.

Data source	Analytical methods	Reference
MEDATLAS	-flow analysis system (autoanalyser) equipped with Chemlab -technicon colorimeters.	http://www.ifremer.fr/mater/dataset_i/chemitt.html
SEADATANET including MOOSE-GE	-flow analysis system (autoanalyser) equipped with Bran-Luebbe Seal	https://www.obs-banyuls.fr/fr/observer/moose.html https://mistrals.sedoo.fr/?editDatsId=1351&datsId=1351&project_name=MOOSE
CNR_DIN_WMED_20042017	-continuous-flow system multichannel (Auto Analyzer Bran+Luebbe III Generation -OI-Analytical (Flow Solution III) flow-segmented -Systea discrete analyzer EasyChem Plus	Belgacem et al., (2020) https://doi.org/10.5194/essd-12-1985-2020
Other cruises: Medship programs; GLODAPv2; CARIMED	nutrient analysis strictly followed the recommendation of the World Ocean Circulation Experiment (WOCE) and the GO-SHIP protocols example: Quaatro auto-analyzer from SEAL analytics.	Schroeder et al., (2015) Tanhua et al., (2013) https://doi.org/10.5194/essd-5-289-2013 Olsen et al., (2016) Hydes et al., (2010)

864

## Appendix B: Additional information about quality assurance

865

866 **Table A2**. Summary of the quality check analysis quality assurance of 1981-2017 climatology.

| RMS	Nitrate	Phosphate	Silicate
Pre-quality check	0.848	0.05	0.763
Post-quality check	**0.838**	**0.049**	**0.757**
Number of suspected points	10	6	2

867
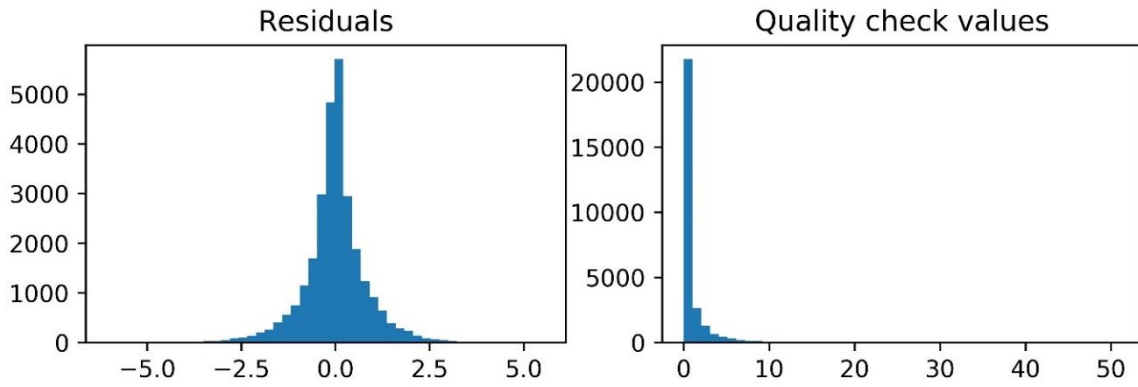
Figure A1. Overview of residual distribution and quality check values for Nitrate gridded fields (1981-2017) before the quality check.

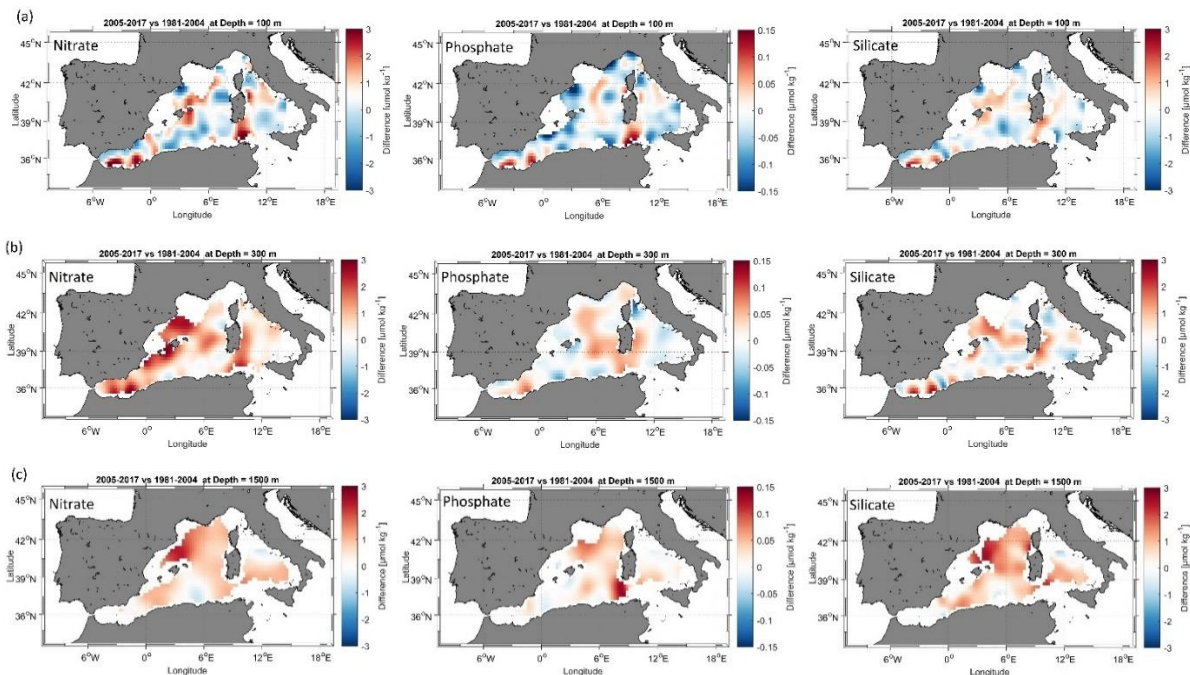
870
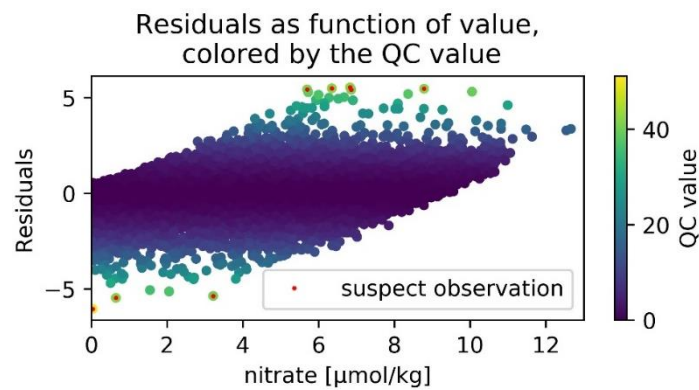
Figure A2. Scatterplot of residual as function of nitrate values (1981-2017) colored by the quality check values. The red dots are the suspect observation (points with qcvalues > 40).

873
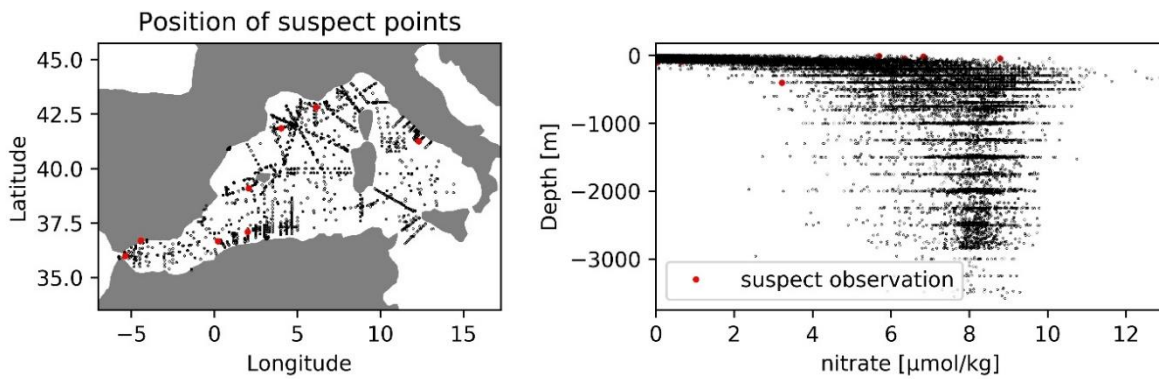
Figure A3. Position of the suspect points (nitrate climatology, 1981-2017).

Appendix C: Additional information about temporal comparison

Figure A4. (a) Difference field at 100 m between the 1981-2004 climatology and the 2005-2017 climatologies; (b) Difference field at 300 m (c) Difference field at 1500.

903

References

Barnes, S.L. (1964). A technique for maximizing details in numerical weather map analysis. J. App. Meteor., 3, 396-409.

Barnes, S.L. (1994). Applications of the Barnes Objective Analysis Scheme, Part III: Tuning for Minimum Error. J. Atmosph. and Oceanic Tech., 11, 1459-1479.

Barth, A., Troupin, C., Alvera-Azcárate, A. and Vandenbulcke, L.: Divand-1.0: N-dimensional variational data analysis for ocean observations, Geosci. Model Dev., 7(1), 225–241, doi:10.5194/gmd-7-225-2014, 2014.

Beckers, J. M., Barth, A., Troupin, C. and Alvera-Azcárate, A.: Approximate and efficient methods to assess error fields in spatial gridding with data interpolating variational analysis (DIVA), J. Atmos. Ocean. Technol., 31(2), 515–530, doi:10.1175/JTECH-D-13-00130.1, 2014.

Belgacem, M., Chiggiato, J., Borghini, M., Pavoni, B., Cerrati, G., Acri, F., Cozzi, S., Ribotti, A., Álvarez, M., Lauvset, S. K. and Schroeder, K.: Dissolved inorganic nutrients in the western Mediterranean Sea (2004-2017), Earth Syst. Sci. Data, 12(3), 1985–2011, doi:10.5194/essd-12-1985-2020, 2020.

Bethoux, J. P., Morin, P., Madec, C. and Gentili, B.: Phosphorus and nitrogen behaviour in the Mediterranean Sea, Deep Sea Res. Part A, Oceanogr. Res. Pap., 39(9), 1641–1654, doi:10.1016/0198-0149(92)90053-V, 1992.

Brankart, J. M. and Brasseur, P.: The general circulation in the Mediterranean Sea: A climatological approach, J. Mar. Syst., 18(1–3), 41–70, doi:10.1016/S0924-7963(98)00005-0, 1998.

Brasseur, P., Beckers, J. M., Brankart, J. M. and Schoenauen, R.: Seasonal temperature and salinity fields in the Mediterranean Sea: Climatological analyses of a historical data set, Deep. Res. Part I Oceanogr. Res. Pap., 43(2), 159–192, doi:10.1016/0967-0637(96)00012-X, 1996.

Brasseur, P. P.: A variational inverse method for the reconstruction of general circulation fields in the northern Bering Sea, J. Geophys. Res., 96(C3), 4891, doi:10.1029/90jc02387, 1991.

Buga, L., Eilola, K., Wesslander, K., Fryberg, L., Gatti, J., Leroy, D., Iona, S., Tsompanou, M. and Lipizer, M.: EMODnet Thematic Lot n ° 4 / SI2 . 749773 Interpolating Variational Analysis (DIVA). Release 2018, , doi:10.6092/A8CFB472-10DB-4225-9737-5A60DA9AF523, 2019.

Capet, A., Troupin, C., Carstensen, J., Grégoire, M. and Beckers, J. M.: Untangling spatial and temporal trends in the variability of the Black Sea Cold Intermediate Layer and mixed Layer Depth using the DIVA detrending procedure, Ocean Dyn., 64(3), 315–324, doi:10.1007/s10236-013-0683-4, 2014.

Crispi, G., Mosetti, R., Solidoro, C. and Crise, A.: Nutrients cycling in Mediterranean basins: The role of the biological pump in the trophic regime, in Ecological Modelling, vol. 138, pp. 101–114., 2001.

Crombet, Y., Leblanc, K., Quéuiner, B., Moutin, T., Rimmelin, P., Ras, J., Claustre, H., Leblond, N., Oriol, L. and Pujo-Pay, M.: Deep silicon maxima in the stratified oligotrophic Mediterranean Sea, Biogeosciences, 8(2), 459–475, doi:10.5194/bg-8-459-2011, 2011.

de Fommervault, O. P., Migon, C., D'Ortenzio, F., Ribera d'Alcalà, M. and Coppola, L.: Temporal variability of nutrient concentrations in the northwestern Mediterranean sea (DYFAMED time-series station), Deep. Res. Part I Oceanogr. Res. Pap., 100, 1–12, doi:10.1016/j.dsr.2015.02.006, 2015.

D'Ortenzio, F. and Ribera d'Alcalà, M.: On the trophic regimes of the Mediterranean Sea: a satellite analysis, Biogeosciences Discuss., 5(4), 2959–2983, doi:10.5194/bgd-5-2959-2008, 2009.

D'Ortenzio, F., Taillandier, V., Claustre, H., Prieur, L. M., Leymarie, E., Mignot, A., Poteau, A.,

946   Penkerc, C. and Schmechtig, C. M.: Biogeochemical Argo : The Test Case of the NAOS Mediterranean
947   Array, , 7(March), 1–16, doi:10.3389/fmars.2020.00120, 2020.

948   DeMaster, D. J.: The accumulation and cycling of biogenic silica in the Southern Ocean: Revisiting the
949   marine silica budget, Deep. Res. Part II Top. Stud. Oceanogr., 49(16), 3155–3167, doi:10.1016/S0967-
950   0645(02)00076-0, 2002.

951   Desroziers, G., Berre, L., Chapnik, B. and Poli, P.: Diagnosis of observation, background and analysis-
952   error statistics in observation space, Q. J. R. Meteorol. Soc., 131(613), 3385–3396,
953   doi:10.1256/qj.05.108, 2005.

954   Diaz, P., Raimbault, F., Boudjellal, B., Garcia, N. and Moutin, T.: Early spring phosphorus limitation
955   of primary productivity in a NW Mediterranean coastal zone (Gulf of Lions), Mar. Ecol. Prog. Ser.,
956   211(McGill 1965), 51–62, doi:10.3354/meps211051, 2001.

957   Fichaut, M., Garcia, M. J., Giorgetti, A., Iona, A., Kuznetsov, A., Rixen, M. and Group, M.:
958   MEDAR/MEDATLAS 2002: A Mediterranean and Black Sea database for operational oceanography,
959   Elsevier Oceanogr. Ser., 69(C), 645–648, doi:10.1016/S0422-9894(03)80107-1, 2003.

960   Frings, P. J., Clymans, W., Fontorbe, G., De La Rocha, C. L. and Conley, D. J.: The continental Si cycle
961   and its impact on the ocean Si isotope budget, Chem. Geol., 425, 12–36,
962   doi:10.1016/j.chemgeo.2016.01.020, 2016.

963   García-Martínez, M. del C., Vargas-Yáñez, M., Moya, F., Santiago, R., Muñoz, M., Reul, A., Ramírez,
964   T. and Balbín, R.: Average nutrient and chlorophyll distributions in the western Mediterranean:
965   RADMED project, Oceanologia, 61(1), 143–169, doi:10.1016/j.oceano.2018.08.003, 2019.

966   Garcia, H. E., Weathers, K. W., Paver, C. R., Smolyar, I., Boyer, T. P., Locarnini, R. A., Zweng, M. M.,
967   Mishonov, A. V., Baranova, O. K., Seidov, D. and Reagan, J. R.: World Ocean Atlas 2018. Vol. 4:
968   Dissolved Inorganic Nutrients (phosphate, nitrate and nitrate+nitrite, silicate)., 2019.

969   Giorgi, F.: Climate change hot-spots, Geophys. Res. Lett., 33(8), 1–4, doi:10.1029/2006GL025734,
970   2006.

971   Hecht, A., Pinardi, N. and Robinson, A. R.: Currents, Water Masses, Eddies and Jets in the
972   Mediterreanean Levantine Basin, J. Phys. Oceanogr., 18(10), 1320–1353, 1988.

973   Houpert, L., Durrieu de Madron, X., Testor, P., Bosse, A., D'Ortenzio, F., Bouin, M. N., Dausse, D., Le
974   Goff, H., Kunesch, S., Labaste, M., Coppola, L., Mortier, L. and Raimbault, P.: Observations of open-
975   ocean deep convection in the northwestern Mediterranean Sea: Seasonal and interannual variability of
976   mixing and deep water masses for the 2007-2013 Period, J. Geophys. Res. Ocean., 121(11), 8139–8171,
977   doi:10.1002/2016JC011857, 2016.

978   Key, R. M., Kozyr, A., Sabine, C. L., Lee, K., Wanninkhof, R., Bullister, J. L., Feely, R. A., Millero, F.
979   J., Mordy, C. and Peng, T. H.: A global ocean carbon climatology: Results from Global Data Analysis
980   Project (GLODAP), Global Biogeochem. Cycles, 18(4), 1–23, doi:10.1029/2004GB002247, 2004.

981   Krom, M. D., Oceanographic, I. and Shikmona, T.: Nutrient budget for the Eastern Mediterranean :
982   Implications for phosphorus limitation, , 49(5), 1582–1592, 2004.

983   Krom, M. D., Emeis, K. C. and Van Cappellen, P.: Why is the Eastern Mediterranean phosphorus
984   limited?, Prog. Oceanogr., 85(3–4), 236–244, doi:10.1016/j.pocean.2010.03.003, 2010.

985   Krom, M. D., Kress, N. and Fanning, K.: Silica cycling in the ultra-oligotrophic eastern Mediterranean
986   Sea, Biogeosciences, 11(15), 4211–4223, doi:10.5194/bg-11-4211-2014, 2014.

987   Lascaratos, A., Roether, W. and Nittis, K.: Recent changes in deep water formation and spreading in the
988   eastern Mediterranean Sea : a review, , 44, 5–36, 1999.

989   Lauvset, S. K., Key, R. M., Olsen, A., Van Heuven, S., Velo, A., Lin, X., Schirnick, C., Kozyr, A.,
990   Tanhua, T., Hoppema, M., Jutterström, S., Steinfeldt, R., Jeansson, E., Ishii, M., Perez, F. F., Suzuki, T.

and Watelet, S.: A new global interior ocean mapped climatology: The $1° \times 1°$ GLODAP version 2, Earth Syst. Sci. Data, 8(2), 325–340, doi:10.5194/essd-8-325-2016, 2016.

Lauvset, S. K., Lange, N., Tanhua, T., Bittig, H. C., Olsen, A., Kozyr, A., Álvarez, M., Becker, S., Brown, P. J., Carter, B. R., Cotrim da Cunha, L., Feely, R. A., van Heuven, S., Hoppema, M., Ishii, M., Jeansson, E., Jutterström, S., Jones, S. D., Karlsen, M. K., Lo Monaco, C., Michaelis, P., Murata, A., Pérez, F. F., Pfeil, B., Schirnick, C., Steinfeldt, R., Suzuki, T., Tilbrook, B., Velo, A., Wanninkhof, R., Woosley, R. J., and Key, R. M.: An updated version of the global interior ocean biogeochemical data product, GLODAPv2.2021, Earth Syst. Sci. Data Discuss. [preprint], https://doi.org/10.5194/essd-2021-234, in review, 2021.

Lavigne, H.: On the vertical distribution of the chlorophyll a concentration in the Mediterranean Sea : a basin scale and seasonal approach, , (March), doi:10.5194/bgd-12-4139-2015, 2015.

Lazzari, P., Solidoro, C., Ibello, V., Salon, S., Teruzzi, A., Béranger, K., Colella, S. and Crise, A.: Seasonal and inter-annual variability of plankton chlorophyll and primary production in the Mediterranean Sea: A modelling approach, Biogeosciences, 9(1), 217–233, doi:10.5194/bg-9-217-2012, 2012.

Lazzari, P., Solidoro, C., Salon, S. and Bolzon, G.: Spatial variability of phosphate and nitrate in the Mediterranean Sea: A modeling approach, Deep. Res. Part I Oceanogr. Res. Pap., 108, 39–52, doi:10.1016/j.dsr.2015.12.006, 2016.

Levitus, S.: Climatological Atlas of the World Ocean, Eos, Trans. Am. Geophys. Union, 64(49), 962–963, doi:10.1029/EO064i049p00962-02, 1982.

Li, P. and Tanhua, T.: Recent Changes in Deep Ventilation of the Mediterranean Sea; Evidence From Long-Term Transient Tracer Observations, Front. Mar. Sci., 7(July), 1–23, doi:10.3389/fmars.2020.00594, 2020.

Lijing, C., Abraham, J., Trenberth, K. E., Fasullo, J., Boyer, T., Locarnini, R., Zhang, B., Yu, F., Wan, L., Chen, X., Song, X., Liu, Y., Mann, M.E., Reseghetti, F., Simoncelli, S., Gouretski, V., Chen, G., Mishonov, A., Reagan, J. and Zhu, J.: Upper ocean temperatures hit record high in 2020, Adv. Atmos. Sci., 38(4), 523–530, https://doi.org/10.1007/s00376-021-0447-x., 2021.

Lipizer, M., Partescano, E., Rabitti, A., Giorgetti, A. and Crise, A.: Qualified temperature, salinity and dissolved oxygen climatologies in a changing Adriatic Sea, Ocean Sci., 10(5), 771–797, doi:10.5194/os-10-771-2014, 2014.

Lucea, A., Duarte, C. M. and Agustı, S.: Nutrient (N , P and Si) and carbon partitioning in the stratified NW Mediterranean, , 49, 157–170, doi:10.1016/S1385-1101(03)00005-4, 2003.

Ludwig, W., Dumont, E., Meybeck, M. and Heussner, S.: River discharges of water and nutrients to the Mediterranean and Black Sea: Major drivers for ecosystem changes during past and future decades?, Prog. Oceanogr., 80(3–4), 199–217, doi:10.1016/j.pocean.2009.02.001, 2009.

Ludwig, W., Bouwman, A. F., Dumont, E. and Lespinas, F.: Water and nutrient fluxes from major Mediterranean and Black Sea rivers: Past and future trends and their implications for the basin-scale budgets, Global Biogeochem. Cycles, 24(4), 1–14, doi:10.1029/2009GB003594, 2010.

Maillard, C., Lowry, R., Maudire, G. and Schaap, D.: SeaDataNet: Development of a Pan-European infrastructure for ocean and marine data management, in OCEANS 2007 - Europe., 2007.

Malanotte-Rizzoli, P., Manca, B. B., D'Alcala, M. R., Theocharis, A., Brenner, S., Budillon, G. and Ozsoy, E.: The Eastern Mediterranean in the 80s and in the 90s: The big transition in the intermediate and deep circulations, Dyn. Atmos. Ocean., 29(2–4), 365–395, doi:10.1016/S0377-0265(99)00011-1, 1999.

Manca, B., Burca, M., Giorgetti, A., Coatanoan, C., Garcia, M. J. and Iona, A.: Physical and biochemical averaged vertical profiles in the Mediterranean regions: An important tool to trace the climatology of water masses and to validate incoming data from operational oceanography, J. Mar. Syst., 48(1–4), 83–

116, doi:10.1016/j.jmarsys.2003.11.025, 2004.

Míguez, B. M., Novellino, A., Vinci, M., Claus, S., Calewaert, J. B., Vallius, H., Schmitt, T., Pititto, A., Giorgetti, A., Askew, N., Iona, S., Schaap, D., Pinardi, N., Harpham, Q., Kater, B. J., Populus, J., She, J., Palazov, A. V., McMeel, O., Oset, P., Lear, D., Manzella, G. M. R., Gorringe, P., Simoncelli, S., Larkin, K., Holdsworth, N., Arvanitidis, C. D., Jack, M. E. M., Chaves Montero, M. del M., Herman, P. M. J. and Hernandez, F.: The European Marine Observation and Data Network (EMODnet): Visions and roles of the gateway to marine data in Europe, Front. Mar. Sci., 6(JUL), 1–24, doi:10.3389/fmars.2019.00313, 2019.

Moon, J., Lee, K., Tanhua, T., Kress, N. and Kim, I.: Temporal nutrient dynamics in the Mediterranean Sea in response to anthropogenic inputs, , 5243–5251, doi:10.1002/2016GL068788.Received, 2016.

Moore, C. M., Mills, M. M., Arrigo, K. R., Berman-Frank, I., Bopp, L., Boyd, P. W., Galbraith, E. D., Geider, R. J., Guieu, C., Jaccard, S. L., Jickells, T. D., La Roche, J., Lenton, T. M., Mahowald, N. M., Marañón, E., Marinov, I., Moore, J. K., Nakatsuka, T., Oschlies, A., Saito, M. A., Thingstad, T. F., Tsuda, A. and Ulloa, O.: Processes and patterns of oceanic nutrient limitation, Nat. Geosci., 6(9), 701–710, doi:10.1038/ngeo1765, 2013.

Murphy, A. H.: Skill Scores Based on the Mean Square Error and Their Relationships to the Correlation Coefficient, Mon. Weather Rev., 116(12), 2417–2424, doi:10.1175/1520-0493(1988)116<2417:SSBOTM>2.0.CO;2, 1988.

Olsen, A., Lange, N., Key, R. M., Tanhua, T., Bittig, H. C., Kozyr, A., Álvarez, M., Azetsu-Scott, K., Becker, S., Brown, P. J., Carter, B. R., Cotrim da Cunha, L., Feely, R. A., van Heuven, S., Hoppema, M., Ishii, M., Jeansson, E., Jutterström, S., Landa, C. S., Lauvset, S. K., Michaelis, P., Murata, A., Pérez, F. F., Pfeil, B., Schirnick, C., Steinfeldt, R., Suzuki, T., Tilbrook, B., Velo, A., Wanninkhof, R., and Woosley, R. J.: An updated version of the global interior ocean biogeochemical data product, GLODAPv2.2020, Earth Syst. Sci. Data, 12, 3653–3678, https://doi.org/10.5194/essd-12-3653-2020, 2020.

Ozer, T., Gertman, I., Kress, N., Silverman, J. and Herut, B.: Interannual thermohaline (1979–2014) and nutrient (2002–2014) dynamics in the Levantine surface and intermediate water masses, SE Mediterranean Sea, Glob. Planet. Change, doi:10.1016/j.gloplacha.2016.04.001, 2017.

Piñeiro, S., González-Pola, C., Fernández-Díaz, J. M. and Balbin, R.: Thermohaline Evolution of the Western Mediterranean Deep Waters Since 2005: Diffusive Stages and Interannual Renewal Injections, J. Geophys. Res. Ocean., 124(12), 8747–8766, doi:10.1029/2019JC015094, 2019.

Pondaven, P., Ruiz-Pino, D., Druon, J. N., Fravalo, C. and Tréguer, P.: Factors controlling silicon and nitrogen biogeochemical cycles in high nutrient, low chlorophyll systems (the Southern Ocean and the North Pacific): Comparison with a mesotrophic system (the North Atlantic), Deep. Res. Part I Oceanogr. Res. Pap., 46(11), 1923–1968, doi:10.1016/S0967-0637(99)00033-3, 1999.

Pujo-Pay, M., Conan, P., Oriol, L., Cornet-Barthaux, V., Falco, C., Ghiglione, J. F., Goyet, C., Moutin, T. and Prieur, L.: Integrated survey of elemental stoichiometry (C, N, P) from the western to eastern Mediterranean Sea, Biogeosciences, 8(4), 883–899, doi:10.5194/bg-8-883-2011, 2011.

Rahav, E., Herut, B., Stambler, N., Bar-Zeev, E., Mulholland, M. R. and Berman-Frank, I.: Uncoupling between dinitrogen fixation and primary productivity in the eastern Mediterranean Sea, J. Geophys. Res. Biogeosciences, 118(1), 195–202, doi:10.1002/jgrg.20023, 2013.

Reale, M., Giorgi, F., Solidoro, C., Di Biagio, V., Di Sante, F., Mariotti, L., Farneti, R. and Sannino, G.: The Regional Earth System Model RegCM-ES: Evaluation of the Mediterranean climate and marine biogeochemistry., 2020.

Reul, A., Rodríguez, V., Jiménez-Gómez, F., Blanco, J. M., Bautista, B., Sarhan, T., Guerrero, F., Ruíz, J. and García-Lafuente, J.: Variability in the spatio-temporal distribution and size-structure of phytoplankton across an upwelling area in the NW-Alboran Sea, (W-Mediterranean), Cont. Shelf Res., 25(5–6), 589–608, doi:10.1016/j.csr.2004.09.016, 2005.

1086 Ribera d'Alcalà, M.: Nutrient ratios and fluxes hint at overlooked processes in the Mediterranean Sea,
1087 J. Geophys. Res., 108(C9), doi:10.1029/2002jc001650, 2003.

1088 Ribera d'Alcalà, M., Civitarese, G., Conversano, F. and Lavezza, R.: Nutrient ratios and fluxes hint at
1089 overlooked processes in the Mediterranean Sea, J. Geophys. Res. Ocean., 108(9),
1090 doi:10.1029/2002jc001650, 2003.

1091 Rixen, M., Beckers, J. M., Brankart, J. M. and Brasseur, P.: A numerically efficient data analysis method
1092 with error map generation, Ocean Model., 2(1–2), 45–60, doi:10.1016/s1463-5003(00)00009-3, 2000.

1093 Roether, W. and Schlitzer, R.: Eastern Mediterranean deep water renewal on the basis of
1094 chlorofluoromethane and tritium data, Dyn. Atmos. Ocean., 15(3–5), 333–354, doi:10.1016/0377-
1095 0265(91)90025-B, 1991.

1096 Roether, W., Manca, Beniamino B. Klein, B., Bregant, D., Georgopoulos, D., Beitzel, V. and
1097 KovaEevic, Vedrana Luchetta, A.: Recent Changes in Eastern Mediterranean Deep Waters., 1996.

1098 Roether, W., Klein, B., Bruno, B., Theocharis, A. and Kioroglou, S.: Progress in Oceanography
1099 Transient Eastern Mediterranean deep waters in response to the massive dense-water output of the
1100 Aegean Sea in the 1990s, , 74, 540–571, doi:10.1016/j.pocean.2007.03.001, 2007.

1101 Roether, W., Klein, B. and Hainbucher, D.: The Eastern Mediterranean Transient: Evidence for Similar
1102 Events Previously?, Mediterr. Sea Temporal Var. Spat. Patterns, 9781118847(January), 75–83,
1103 doi:10.1002/9781118847572.ch6, 2014.

1104 Salgado-Hernanz, P. M., Racault, M. F., Font-Muñoz, J. S. and Basterretxea, G.: Trends in
1105 phytoplankton phenology in the Mediterranean Sea based on ocean-colour remote sensing, Remote
1106 Sens. Environ., 221(October 2018), 50–64, doi:10.1016/j.rse.2018.10.036, 2019.

1107 Sarmiento, J. L. and Toggweiler, J. R.: A new model for the role of the oceans in determining
1108 atmospheric PCO 2, Nature, 308(5960), 621–624, doi:10.1038/308621a0, 1984.

1109 Schröder, K., Gasparini, G. P., Tangherlini, M. and Astraldi, M.: Deep and intermediate water in the
1110 western Mediterranean under the influence of the Eastern Mediterranean Transient, Geophys. Res. Lett.,
1111 33(21), 2–7, doi:10.1029/2006GL027121, 2006.

1112 Schroeder, K., Gasparini, G. P., Borghini, M., Cerrati, G. and Delfanti, R.: Biogeochemical tracers and
1113 fl uxes in the Western Mediterranean Sea , spring 2005, J. Mar. Syst., 80(1–2), 8–24,
1114 doi:10.1016/j.jmarsys.2009.08.002, 2010.

1115 Schroeder, K., Tanhua, T., Bryden, H., Alvarez, M., Chiggiato, J. and Aracri, S.: Mediterranean Sea
1116 Ship-based Hydrographic Investigations Program (Med-SHIP), Oceanography, 28(3), 12–15,
1117 doi:10.5670/oceanog.2015.71, 2015.

1118 Schroeder, K., Chiggiato, J., Bryden, H. L., Borghini, M. and Ismail, S. Ben: Abrupt climate shift in the
1119 Western Mediterranean Sea, Nat. Publ. Gr., 1–7, doi:10.1038/srep23009, 2016.

1120 Schroeder, K., Chiggiato, J., Josey, S. A., Borghini, M., Aracri, S. and Sparnocchia, S.: Rapid response
1121 to climate change in a marginal sea, , (May), 1–7, doi:10.1038/s41598-017-04455-5, 2017.

1122 Schroeder, K., Cozzi, S., Belgacem, M., Borghini, M., Cantoni, C., Durante, S., Petrizzo, A., Poiana, A.
1123 and Chiggiato, J.: Along-Path Evolution of Biogeochemical and Carbonate System Properties in the
1124 Intermediate Water of the Western Mediterranean, Front. Mar. Sci., 7(May), 1–19,
1125 doi:10.3389/fmars.2020.00375, 2020.

1126 Shepherd, J. G., Brewer, P. G., Oschlies, A. and Watson, A. J.: Ocean ventilation and deoxygenation in
1127 a warming world: posters, Philos. Trans. R. Soc. A Math. Phys. Eng. Sci., 375(2102), 20170241,
1128 doi:10.1098/rsta.2017.0241, 2017.

1129 Sospedra, J., Niencheski, L. F. H., Falco, S., Andrade, C. F. F., Attisano, K. K. and Rodilla, M.:
1130 ScienceDirect Identifying the main sources of silicate in coastal waters of the Southern Gulf of Valencia

1131 (Western Mediterranean Sea), Oceanologia, 60(1), 52–64, doi:10.1016/j.oceano.2017.07.004, 2018.

1132 Stöven, T. and Tanhua, T.: Ventilation of the mediterranean sea constrained by multiple transient tracer
1133 measurements, Ocean Sci., 10(3), 439–457, doi:10.5194/os-10-439-2014, 2014.

1134 Tanhua, T., Hainbucher, D., Schroeder, K., Cardin, V., Álvarez, M. and Civitarese, G.: The
1135 Mediterranean Sea system: A review and an introduction to the special issue, Ocean Sci., 9(5), 789–
1136 803, doi:10.5194/os-9-789-2013, 2013.

1137 Testor, P., Bosse, A., Houpert, L., Margirier, F., Mortier, L., Legoff, H., Dausse, D., Labaste, M.,
1138 Karstensen, J., Hayes, D., Olita, A., Ribotti, A., Schroeder, K., Chiggiato, J., Onken, R., Heslop, E.,
1139 Mourre, B., D'ortenzio, F., Mayot, N., Lavigne, H., de Fommervault, O., Coppola, L., Prieur, L.,
1140 Taillandier, V., Durrieu de Madron, X., Bourrin, F., Many, G., Damien, P., Estournel, C., Marsaleix, P.,
1141 Taupier-Letage, I., Raimbault, P., Waldman, R., Bouin, M. N., Giordani, H., Caniaux, G., Somot, S.,
1142 Ducrocq, V. and Conan, P.: Multiscale Observations of Deep Convection in the Northwestern
1143 Mediterranean Sea During Winter 2012–2013 Using Multiple Platforms, J. Geophys. Res. Ocean.,
1144 123(3), 1745–1776, doi:10.1002/2016JC012671, 2018.

1145 Theocharis, A., Lascaratos, A. and Sofianos, S.: Variability of sea water properties in the Ionian , Cretan
1146 and Levantine seas during the last century, , (April), 22–24, 2002.

1147 Troupin, C., MacHín, F., Ouberdous, M., Sirjacobs, D., Barth, A. and Beckers, J. M.: High-resolution
1148 climatology of the northeast Atlantic using Data-Interpolating Variational Analysis (Diva), J. Geophys.
1149 Res. Ocean., 115(8), 1–20, doi:10.1029/2009JC005512, 2010.

1150 Troupin, C., Barth, A., Sirjacobs, D., Ouberdous, M., Brankart, J. M., Brasseur, P., Rixen, M., Alvera-
1151 Azcárate, A., Belounis, M., Capet, A., Lenartz, F., Toussaint, M. E. and Beckers, J. M.: Generation of
1152 analysis and consistent error fields using the Data Interpolating Variational Analysis (DIVA), Ocean
1153 Model., 52–53, 90–101, doi:10.1016/j.ocemod.2012.05.002, 2012.

1154 Troupin, C., Watelet, S., Ouberdous, M., Sirjacobs, D., Barth, A., Toussaint, M. and Beckers, J.: Data
1155 Interpolating Variational Analysis User Guide, , 836723, doi:10.5281/zenodo.836723, 2018.

1156 Van Cappellen, P., Powley, H. R., Emeis, K. C. and Krom, M. D.: A biogeochemical model for
1157 phosphorus and nitrogen cycling in the Eastern Mediterranean Sea: Part 1: Model development,
1158 initialization and sensitivity, J. Mar. Syst., 139, 460–471, doi:10.1016/j.jmarsys.2014.08.016, 2014.

1159 Vargas-yáñez, M.: Updating temperature and salinity mean values and trends in the Western
1160 Mediterranean : The RADMED project Progress in Oceanography Updating temperature and salinity
1161 mean values and trends in the Western Mediterranean : The RADMED project, Prog. Oceanogr.,
1162 157(September), 27–46, doi:10.1016/j.pocean.2017.09.004, 2017.

1163 Weatherall, P., Marks, K. M., Jakobsson, M., Schmitt, T., Tani, S., Arndt, J. E., Rovere, M., Chayes, D.,
1164 Ferrini, V. and Wigley, R.: A new digital bathymetric model of the world's oceans, Earth Sp. Sci., 2,
1165 331–345, doi:doi: 10.1002/ 2015EA000107, 2015.

1166 Williams, R. G. and Follows, M. J.: Physical Transport of Nutrients and the Maintenance of Biological
1167 Production, in Ocean Biogeochemistry, pp. 19–51., 2003.

1168